

3D NUMERICAL MODELS FOR ALONG-AXIS VARIATIONS IN DIKING AT
MID-OCEAN RIDGES

by

Xiaochuan Tian

A Thesis

Submitted in Partial Fulfillment of the
Requirements for the Degree of
Master of Science

Major: Geophysics

The University of Memphis

May, 2015

Copyright © 2015 Xiaochuan Tian

All rights reserved

Dedication

I would like to dedicate this Thesis to my mother, Xia Tian, the most important person in my life. Without her guidance and support, I will not become who I am.

Acknowledgements

To Eunseo,
To Committee members,
To CERI,

Abstract

Tian, Xiaochuan. M.S. The University of Memphis. May 2015. 3D Numerical Models for Along-axis Variations in Diking at Mid-Ocean Ridges. Major Professor: Eunseo Choi.

Bathymetry of ocean floors reveals a great variety of morphologies at Mid-ocean Ridges (MORs). Previous studies showed that the morphologies at slow spreading MORs are mainly controlled by the ratio between rates of magma supply and plate extension. 2D models for the across-ridge cross-sections have been successful in explaining many of the observed morphological features such as abyssal hills and oceanic core complexes. However, the magma supply varies along the ridge and the interaction between the tectonic plates and magmatism at MORs are inevitably 3D processes. We propose to investigate the consequences of the along-axis variability in diking in terms of faulting pattern and the associated structures. This work will include implementation of an algorithm of parameterizing repeated diking in a 3D parallel geodynamic modeling code.

Table of Contents

Chapter	Page
1 Introduction	1
1.1 Research Questions	1
1.2 Review of Literature	1
1.3 Statement of Research Purpose	5
1.4 Findings	6
2 Methods	7
2.1 Method of approach	7
2.2 Model Setup	9
2.3 Parameters to control	10
3 3D Results	12
3.1 Reference models	12
3.1.1 M varies along the ridge-axis (M28LinT1 Table 2)	12
3.1.2 Constant M along the ridge-axis	16
3.2 Tables of all the data points	17
3.3 Variation of the functional form	18
3.3.1 Comparing M28 in terms of linear, sinusoidal and square root	18
3.4 Influence of weakening rate	20
3.4.1 M57SinT1 versus M57SinT2	21
3.4.2 M58SinT1 versus M58SinT2	24
3.4.3 M58SqrtT1 versus M58SqrtT2	26
3.5 Variation of the range of M	28
3.5.1 M28SinT1 versus M57SinT1 versus M58SinT1	29
3.5.2 M57SinT2 versus M58SinT2	30

3.5.3	M28LinT1 versus M57LinT1	30
3.5.4	M28SqrtT1 versus M58SqrtT1	32
3.5.5	M57SqrtT2 versus M58SqrtT2	32
3.6	Summary of Results	33
4	Discussion	36
4.1	Discussion on Reference models	37
4.1.1	Location of termination (M28LinT1)	37
4.1.2	Shear low (M28LinT1)	38
4.2	Cut Back	39
4.3	Faulting Patterns Evolution	44
4.3.1	Trade-off between bending and weakening	44
4.3.2	Alternating on conjugate plate	46
4.3.3	Secondary near-axis normal fault	46
4.4	Corrugations	46
4.4.1	Wavelength of corrugations	47
4.5	Influence of healing	47
4.6	Comparing model results with nature observation	47
4.7	Parallel computing efficiency	47
4.8	Model Limitation	47
4.8.1	Fixed thermal structure effects and justification	47
4.9	Reccomendation for Future Research	47
5	Conclusions	48

List of Tables

1	Summary of 3D Model Parameters	11
2	List of 3D numerical experiments. M28LinT1 and M88ConT2 are the two reference models.	17
3	Model behaviors in short.	34
4	Linear functional form.	34
5	Sinusoidal functional form.	34
6	Square root functional form.	35

List of Figures

1	Profiles of bathymetry across MORs.	2
2	Two bathymetry cross-sections of Mid-Atlantic Ridge (MAR) with 10 times vertical exaggeration. A-A' is closer to the ridge segment center while B-B' is at the tip of the segment near the Atlantis Transform fault.	2
3	Relationship between the maximum crustal thickness variations along a ridge segment and the segment length. The dashed line is the best-fit linear regression of the combined data. [Chen and Lin, 1999]	3
4	Upper one: modeling result for fast spreading agrees well with the observation of East Pacific Rise. Lower one: modeling result for slow spreading ridges agrees well with the bathymetry of Mid Atlantic Ridge. [Buck et al., 2005]	4
5	A~F: Faulting behavior for different values of M. Geologic interpretation is superimposed on modeled distribution of strain rate. Dots show breakaways of initial faults. Dashed seafloor is original model seafloor, red dotted seafloor is formed dominantly by magmatic accretion, and solid bold is fault surface. Note that detachment faults in B and C are not interrupted by secondary faults. [Tucholke et al., 2008]	5
6	Essential components of the numerical method to be used for the proposed research	8
7	Model setup	9

8	Reference model one: M linearly increases from 0.2 to 0.8 from front to back, Type one weakening (M28LinT1) (Table 2). The top layer is the topography of the model with five times vertical exaggeration. The color scale within Figure 8.a is for the topography. Initial seafloor is marked as a reference of zero km in height. The green, yellow and red colors in the background of blue model domain are plastic strain. Its color scale is shown in Figure 8.e. The number with kyr as a unit beneath each model result is the time for the model with a unit of thousands of year. The two insets in Figure 8.b and Figure 8.d is for stress σ_{xx} (S_{xx} in the figure). Positive value (pink and red) means tension and negative (blue) is compression. The inset in Figure 8.h is for shear stress σ_{xz} (S_{xz} in the figure). It share the same color scale with insets in the Figure 8.b and Figure 8.d. The inset in Figure 8.f is a transparent view of plastic strain. The inset in Figure 8.g shows both plastic strain and the velocity vector. Indicated by the velocity vector, the hanging wall of the detachment fault at low M region ($M0.2\sim M0.5$) is moving in an opposite direction to the hanging wall at higher M region ($M > 0.5$).	13
9	M88ConT2 (Table 2). Reference model two: constant $M= 0.8$ along the ridge-axis (i.e. Z axis). Type two weakening.	16
10	Three functional forms of M variation comparison. They begin to exceed the $M= 0.5$ black line at $Z=10, 7, 5$ for linear, sinusoidal and square root respectively.	18
11	M28LinT1 versus M28SinT1 (Table 2). Secondary fault length comparison between linear and sinusoidal. Around 13 elements in length for sinusoidal compared to 11 elements for linear.	19
12	M28LinT1 versus M28SqrtT1 (Table 2) at 97kyr. View from top of the model.	20

13	M28LinT1 versus M28SqrtT1 (Table 2) at 100kyr. View from top of the model.	21
14	M57SinT2 versus M57SinT1 (Table 2). a) and b) are for M57SinT2, c) and d) are for M57SinT1.	22
15	M57SinT1 (Table 2) faulting and stress evolution with respect to time. . . .	22
16	M57SinT2 (Table 2) faulting and stress evolution with respect to time. . . .	23
17	M58SinT1 (Table 2) faulting and stress evolution with respect to time. . . .	24
18	M58SinT2 (Table 2) faulting and stress evolution with respect to time. . . .	26
19	M58SqrtT1 (Table 2) faulting and stress evolution with respect to time. . . .	27
20	M58SqrtT2 (Table 2) faulting and stress evolution with respect to time. . . .	28
21	M28SinT1 (Table 2) faulting and stress evolution with respect to time. . . .	29
22	M57LinT1 (Table 2) faulting and stress evolution with respect to time. . . .	31
23	M57SqrtT2 (Table 2) faulting and stress evolution with respect to time. . . .	33
24	M28LinT1 (Table 2). Strain rate at 107.5kyr with five slices along ridge axis(Z axis).	38
25	M28LinT1 (Table 2). Breakaway evolution through time. Viewing from top. Left column is topography at different time; Right column is plastic strain. They both share same color scales in the figure 8. The offset between breakways along the ridge-axis in X-axis direction remains three elements until time 295kyr. It also shows that the lowest topography points along the ridge-axis start as a straight line parallel with ridge-axis in a) and then gradually become oblique to the ridge-axis. Please see text for detail description.	39
26	M28SqrtT1 (Table 2). Cut back behaviors in square root functional form model with different time.	40

27	M28SqrtT1 (Table 2). Square root functional form model at 160kyr. Pre- accumulated shear zone increase the shear force and cut the weak detachment front tip	41
28	Bending stress illustration. The blue line is the neutral plane where $\sigma_{xx} = 0$. Above the neutral plane is compression and beneath it is tension. Due to sea water pressure and lithostatic pressure, compression is generally one degree magnitude larger than tension.	41
29	M28SqrtT1 (Table 2). Bending stress drop in the crust close to dike due to cut back behavior.	42
30	M28SqrtT1 (Table 2). New fault front chase after initial abandoned break-away.	43
31	M28SqrtT1 (Table 2). Higher σ_{xx} in the median valley of conjugate plate at low M side.	44
32	Trade-off between change in bending force ΔF_b and weakening in the fault interface ΔF_w . H is the thickness of the brittle crust and γ is the size of initial weak perturbation and A defines the maximum bending force change. (For more details, please refer to [Lavier et al., 2000])	45

1 Introduction

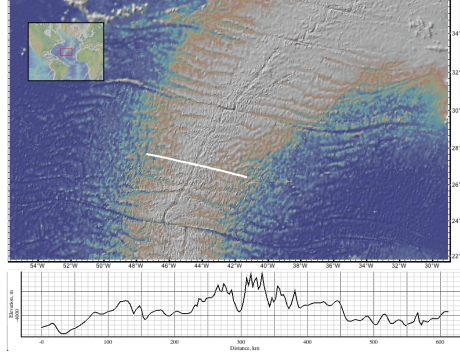
Around 70% of the Earth's crust is oceanic crust and the mid-ocean ridges (MORs), the longest mountain chains on the Earth, are where new crust are forming with a multitude of seismic and volcanic activities. To study how new crust is created and how MORs evolve is significant for Earth Sciences. Geodynamic modeling along with a variety of geological, geophysical observation and lab experiment constraints have been used to study how the MORs work as a system under geological time scale.

1.1 Research Questions

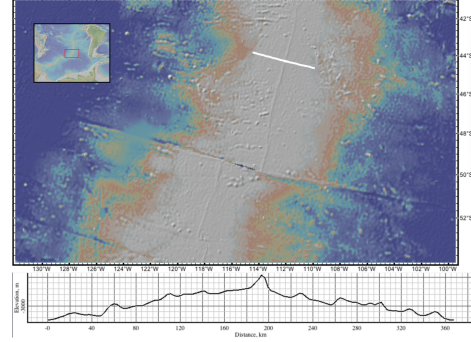
High-resolution multi-beam bathymetry has revealed various characteristics of topography along and across MOR axis. Three specific questions stimulate people's interests most. First, what causes the distinct difference in axial topography between slow and fast spreading ridges. Second, for slow spreading ridges, why does topography along ridge varies and how to explain many features observed. Third, why do oceanic core complexes (OCCs) form and what is the mechanism.

1.2 Review of Literature

According to [Fowler, 2004], variations in mid-ocean ridge morphologies are mainly controlled by four factors: magma supply, tectonic strain, hydrothermal circulation and spreading rate. Among them, the spreading rate is the most important. Slow-to-intermediate spreading centers (half spreading rate less than 4cm/year) produce median valleys that are typically 10~20km wide and 1~2km deep (e.g., Mid-Atlantic Ridges, Figure 1(a)). Fast-spreading centers (half spreading rate greater than 5cm/year) have axial highs that are 10~20 km wide, 0.3~0.5 km high (e.g., East Pacific Rise, Figure 1(b)).



(a) Slow spreading Mid-Atlantic Ridge



(b) Fast spreading East Pacific Rise

Figure 1: Profiles of bathymetry across MORs.

Slow spreading ridges exhibit along-axis variations as well in terms of the width and depth of median valleys and the off-axis morphology. Figure 2 shows that the topographic profile nearer to the center of the ridge segment (A-A') is rather symmetric and has higher frequency. The maximum relief is about 1km. In contrast, the near-tip profile (B-B') is asymmetric and has much lower frequency and a greater relief ($\sim 3\text{km}$). The bathymetry and crustal thickness along the ridge valley also varies. From [Chen and Lin, 1999], the maximum along-axis variation in crustal thickness ΔH_c is linearly increasing with segment length L , and the relationship is $\Delta H_c(L) = 0.0206L$ (Figure 3).

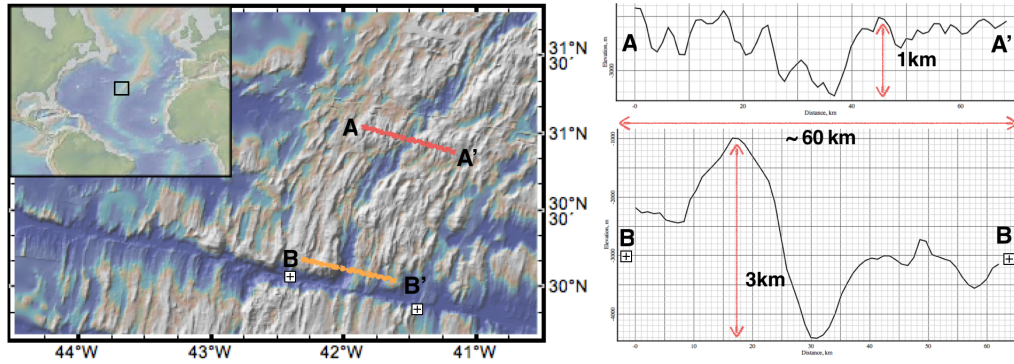


Figure 2: Two bathymetry cross-sections of Mid-Atlantic Ridge (MAR) with 10 times vertical exaggeration. A-A' is closer to the ridge segment center while B-B' is at the tip of the segment near the Atlantis Transform fault.

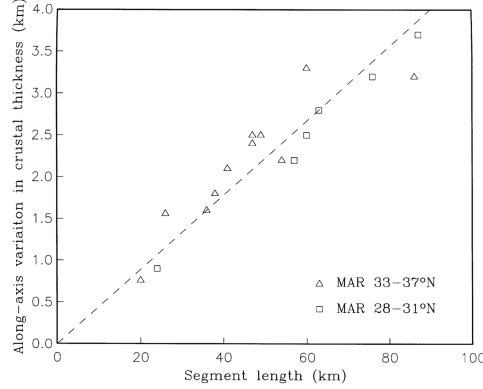


Figure 3: Relationship between the maximum crustal thickness variations along a ridge segment and the segment length. The dashed line is the best-fit linear regression of the combined data. [Chen and Lin, 1999]

Magma supply at MORs is mostly a passive process when no hot plume presents [Fowler, 2004]. Hot mantle rises up to fill the vacated room being created by plate separation and decompression will lead to partial melting of the hot mantle. The melt upwells due to both pressure difference and buoyancy from lateral density difference. When the melt solidifies near the surface, it forms new crust. This diking process can also release extensional stresses result from far-field driving forces.

The passive nature of magma supply results in the major difference between fast and slow spreading ridges in the amount of magma supply. At the fast spreading ridges, magma supply is always sufficient for accommodating plate separation by filling the space by dikes. However, the amount of magma supplied in the form of dikes is not as much at slow spreading ridges and the oceanic lithosphere experiences internal deformations (i.e. tectonics process like normal faulting) when the accumulated extensional stress exceeds the strength of the crust.

Buck et al. [2005] attributed the contrasting faulting patterns and ocean floor morphology of fast- and slow-spreading ridges to the difference in the amount of plate extension accommodated by diking. They defined the ratio between the rates of diking and plate separation as $M = V_{dx}/2V_x$, where V_{dx} is the extensional velocity of a widening dike and V_x is the half spreading rate of the MOR. According to this definition, $M = 1$ represents the case

where diking is frequent enough to release all the tensional stresses from plate separation. $M = 0$ corresponds to the case of no magma supply, in which diking does not account for any of the plate motion and therefore plates kinematics requires plates to go through internal deformations. As shown in Figure 4, an axial high forms at a fast spreading ridge ($M=1$) due to buoyancy from lateral density difference across ridge axis but a median valley forms at a slow-spreading ridge ($M=0.5$) due to near-axis normal faulting, which is in turn caused by the stretching of oceanic lithosphere.

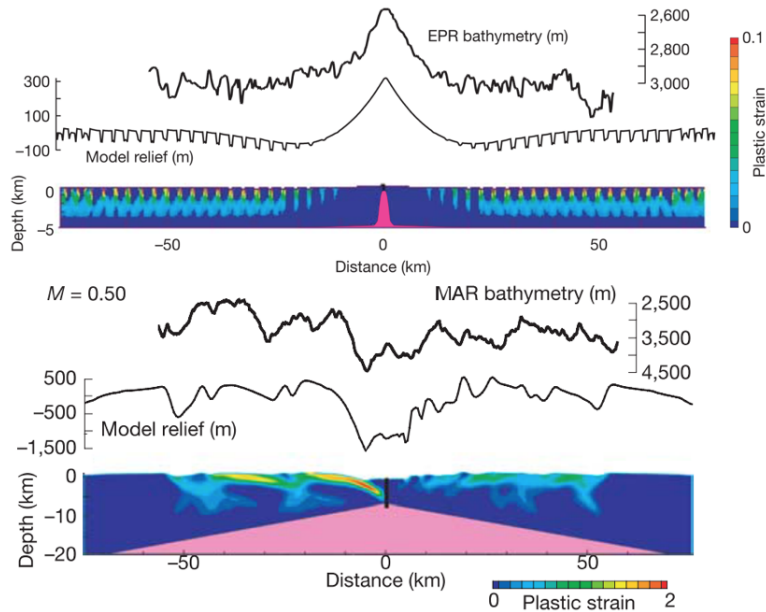


Figure 4: Upper one: modeling result for fast spreading agrees well with the observation of East Pacific Rise. Lower one: modeling result for slow spreading ridges agrees well with the bathymetry of Mid Atlantic Ridge. [Buck et al., 2005]

Tucholke et al. [2008] expanded the investigation on the role of M in the mid-ocean ridge mechanics. They focused on faulting behaviors of slow spreading ridges and find that the OCCs are most likely to form when M varies from 0.3 to 0.5. As shown in Figure 5, when $M=0.7$, repeated diking pushes faults forming at the spreading center away from axis. Since the thickness of the brittle layer increases away from the ridge axis, frictional and bending energy for maintaining the fault also increases. When it exceeds the energy for breaking a new near-axis fault, the old fault will be replaced by the new one. When

$M=0.3\sim0.5$, the normal faults remains active for a long time to become detachment faults, exhuming the lower crust and mantle materials to the seafloor. When M is less than 0.3, most of the tension is accommodated by intra-plate deformations rather than by diking and as a result, faulting pattern is more complicated and unsteady.

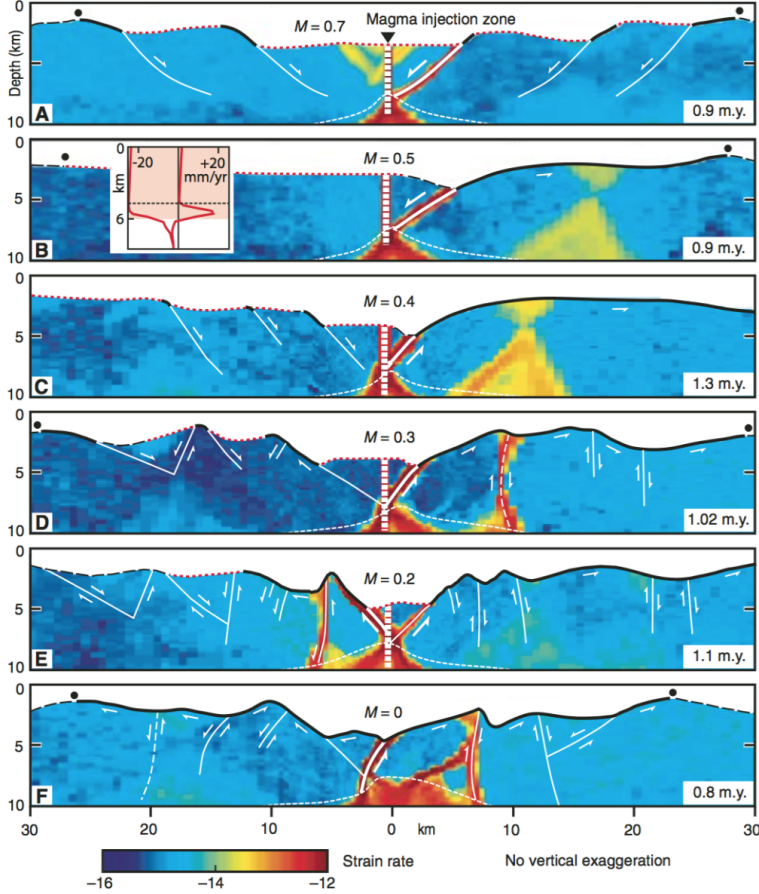


Figure 5: A~F: Faulting behavior for different values of M . Geologic interpretation is superimposed on modeled distribution of strain rate. Dots show breakaways of initial faults. Dashed seafloor is original model seafloor, red dotted seafloor is formed dominantly by magmatic accretion, and solid bold is fault surface. Note that detachment faults in B and C are not interrupted by secondary faults. [Tucholke et al., 2008]

1.3 Statement of Research Purpose

The M -factor formulation used in these previous 2D models successfully explained major features found in across-ridge profiles of seafloor bathymetry. However, 2D models have limitations in studying the along ridge-axis interactions, especially when important variables are not constant along the ridge axis. Magma supply at fast spreading ridges seems always sufficient for accommodating plate motions with little variation along the ridge axis. The relatively uniform topography along fast spreading ridges is considered to be consis-

tent with the uniformly abundance of magma supply. However, along the slow spreading ridges, bathymetry, gravity anomaly and results from reflection and refraction seismology show good correlation with variation in crustal thickness [Ryan et al., 2009, Chen and Lin, 1999, Lin et al., 1990, Tolstoy et al., 1993]. Because oceanic crust is mainly formed by upwelled magma at the ridge, variation in the thickness of the crust implies variation in magma supply. At slow spreading ridges, hydrothermal cooling, thermal structures and even local spreading rate [Baines et al., 2008] also varies both along and across the ridge axis and they appear interrelated. Thus, for slow-to-intermediate spreading ridges, the interactions between tectonics and magmatism at MORs are inevitably 3D processes and 3D numerical models are desirable for better understanding factors controlling both across-and along-ridge variations.

1.4 Findings

2 Methods

The purpose of this thesis is to study how the along-ridge variation in M will make a contribution to the observed various topography assuming that M is the first order control over the topography evolution of MORs governing the interaction between magmatism and tectonic deformations. We will extend the M-factor formulation originally developed for 2D models to 3D by implementing it into a 3D numerical modeling code SNAC [[Choi et al., 2008](#)]. We will focus on studying the last two questions mentioned in the introduction: 1) why does topography along ridge varies and how to explain many features observed; 2) why do OCCs form and what is the mechanism.

By systematically exploring the behaviors of the 3D models and comparing them with observations, we will be able to better understand how the mid-ocean ridge magmatism and tectonic deformations interact.

2.1 Method of approach

The numerical modeling code, SNAC, is an explicit Lagrangian finite element code. It solves the force balance equation for elasto-visco-plastic materials. Figure 6 shows major parts of the SNAC's algorithm.

For each time step dt , strain and strain rates are updated based on the boundary conditions shown in Figure 7. A constitutive model returns updated stresses corresponding to these deformation measures. Internal forces are then calculated from the update stresses, which is plugged into the momentum balance equation together with the body force term. Then, the net force divided by internal mass yields acceleration at a node point, which is time-integrated to velocity and displacement.

A 3D domain is discretized into hexahedral elements, each of which is in turn divided into two sets of tetrahedra. This symmetric discretization prevents faulting from favoring a specific direction or “mesh grains”.

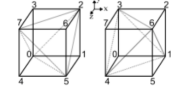
Rheology for the oceanic lithosphere is assumed to be elasto-visco-plastic. When viscosity is high at low temperature, the rheology essentially becomes the Mohr-Coulomb plasticity with strain softening and thus can create shear bands that behave like faults. Strain softening is realized by cohesion decreasing with increasing amount of permanent (i.e., plastic) strain. We assume this relationship is linear for simplicity such that it is sufficient for a full description of strain weakening to define initial and final values of cohesion and a critical plastic strain at which cohesion becomes the final value. We define the rate of strain weakening as the cohesion difference divided by the critical plastic strain and use it as one of the model parameters. When temperature is high and viscosity is low, the rheology becomes the Maxwell viscoelasticity and can model creeping flow. By assuming an appropriate initial temperature distribution, we can effectively set up a structure of a brittle lithosphere and a ductile asthenosphere. Rheological parameters are taken from previous studies that used a similar rheology [Buck 2005; Tuckholke et al., 2008] or from lab experiments [e.g., Kirby and Kronenberg, 1987].

For 3D diking processss, the expanding strain $\Delta\varepsilon_{xx}$ results from diking at the ridge will lead to extra-stresses in all three directions $\Delta\sigma_{xx}$, $\Delta\sigma_{yy}$ and $\Delta\sigma_{zz}$ based on the constitutive equations $\sigma_{ij} = \delta_{ij}\lambda\varepsilon_{ij} + 2\mu\varepsilon_{ij}$.

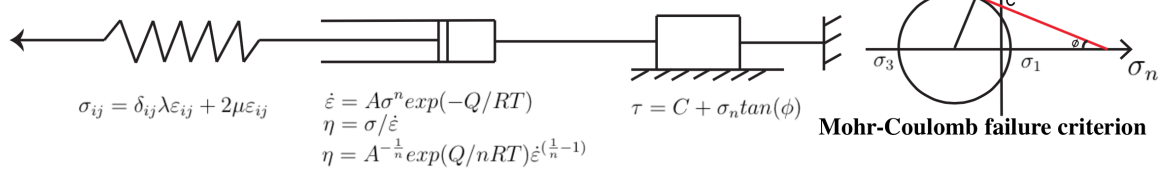
SNAC: a 3D, MPI parallelized, updated Lagrangian explicit finite difference code for modeling long-term tec-tonic evolution of the Earth's elasto-visco-plastic crust and mantle. (Choi et al., 2008)

Momentum Balance Equation: $\frac{\partial\sigma_{ij}}{\partial x_j} + \rho g_i = \rho \frac{Dv_i}{Dt}$

Spatial Decritization: A 3D domain is discretized into hexahedral elements, each of which is filled with two sets of 5 tetrahedra.



Elasto-Visco-Plastic (EVP) Rheology:



Diking M Formulation: $\text{M= } Vdx / 2Vx$ (Vdx is the dike accretion strain(dike widening) $\Delta\varepsilon_{xx}$ in each time step dt)

Stresses introduced by a dike accretion strain(dike widening) $\Delta\varepsilon_{xx}$ in each time step dt:

$$\Delta\sigma_{xx} = (\lambda + 2\mu)\Delta\varepsilon_{xx} \quad \Delta\sigma_{yy} = \lambda\Delta\varepsilon_{xx} \quad \Delta\sigma_{zz} = \lambda\Delta\varepsilon_{xx}$$

Figure 6: Essential components of the numerical method to be used for the proposed research

2.2 Model Setup

^{XT:} Add a table for parameters in use. The 3D models has a geometry of $(60\text{km} \times 20\text{km} \times 20\text{km})$ in X, Y and Z axes respectively with a resolution of $\text{dx} = 1\text{km}$ (dx is the length scale for each hexahedron element). For pseudo-2D models, they have a geometry of $(60\text{km} \times 20\text{km} \times 1\text{km})$ in X, Y and Z axes respectively with a resolution of $\text{dx} = 0.5\text{km}$. As shown in Figure 7, temperature linearly increases from 0°C at the top surface to 240°C at the depth of 6 km, reflecting enhanced cooling due to hydrothermal circulation. Below 6 km, the temperature profile follows the semi-infinite half-space cooling model of moving plates [e.g., Turcotte and Schubert, 2002]. Two sides perpendicular to the z coordinate axis are free-slip. The top surface has a vertical traction from water column, of which height is locally determined as $4000-h(x,z)$ m, where $h(x,z)$ is the topography at a location, (x,z) . The bottom surface is supported by the Winkler foundation. Temperature is fixed at 0°C on the top surface and at 1300°C on the bottom surface. We will adopt the power-law rheology of dry diabase[e.g., Kirby and Kronenberg, 1987, Buck et al., 2005].

For detail model parameters, please refer to Table 1.

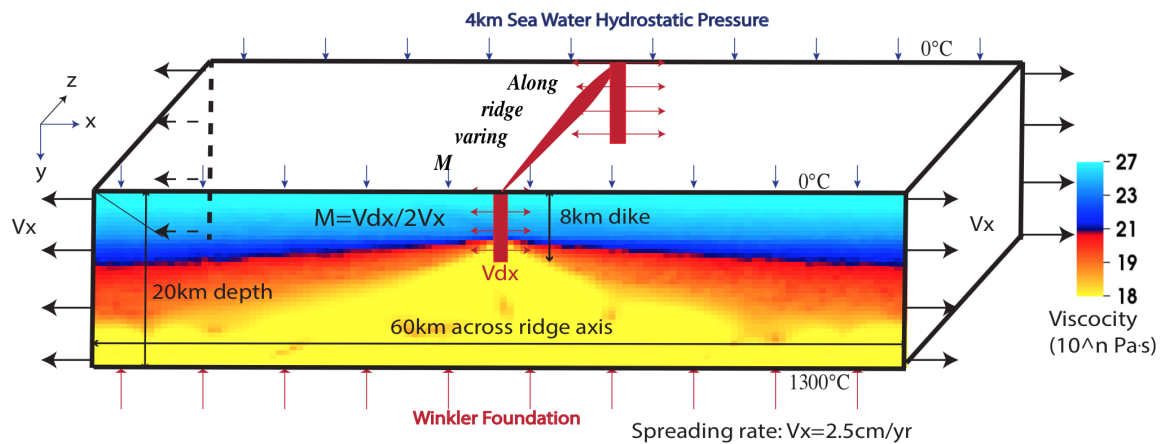


Figure 7: Model setup

2.3 Parameters to control

Although how to estimate the M values from observations has not been well established, we do have constraints from a large dataset of bathymetry, gravity and seismic surveys as well as geological drilling. Generally, at slow spreading ridges, magma supplies mostly at the center of the ridge segment and decreases towards the end of the segment [Tolstoy et al., 1993, Chen and Lin, 1999]. There is also evidence for shorter wavelength of 10 to 20 km discrete focus of magma accretion along the ridge axis [Lin et al., 1990].

Based on these constraints, we can start considering only a few end-member scenarios of variations in M along the ridge axis. The variation in M is parametrized in terms of the functional forms (e.g. discrete increment, linear, sinusoidal and square root), its wavelength (e.g. 10km, 20km and 40km) and the ranges of M (e.g. 0.2 to 0.8, 0.5 to 0.7 and 0.5 to 0.8).

Preliminary pseudo-2D results show that the model behavior in faulting pattern is sensitive to the rate of strain weakening. Two cases of strain weakening are tested in this study. In one case (denoted as Type 1), cohesion linearly decreases from 44 MPa (denoted as C_i) to 4 MPa (C_e) for plastic strain accumulating from 0 (ε_{p_i}) to 0.1 (ε_{p_e}). It has a characteristic fault slip of 150 meters for pseudo-2D models and 300 meters for 3D models. The other case (Type 2) assumes cohesion linearly decreasing from 44 MPa to 4 MPa for plastic strain accumulating from 0 to 0.33. In this case, the characteristic fault slip for Pseudo-2D models is 500 meters and for 3D models is 1km.

The characteristic fault slip $\Delta X_c = 3 \times dx \times \varepsilon_{p_e}$ (3 is because the thickness of the shear bands is usually 2 to 4 times of the dx [Lavier et al., 2000]) means when ΔX_c amount of displacement takes place at the fault interface, the Cohesion of the material at the faulting interface will decrease to C_e . In this way, under same amount of ΔX_c , models with different resolution should behave in the same way in terms of strain weakening and faulting patterns.

Number	Variable	Description	Value	Units
1	W_{dike}	Dike width	2	km
2	D_{dike}	Dike depth	8	km
3	H	Crustal thickness at dike	6	km
4	dT/dy	Crustal thermal gradient	40	K/km
5	T_1	Temperature at lower boundary of crust	240	°C
6	g	Gravity acceleration	10	m/s ²
7	$demf$	Dimensionless force damping factor	0.8	N/A
8	dt	Time step	1.5768e+07	second
9	$topokappa$	Parameter for topography smoothing	0	N/A
10	$shadowDepth$	Ghost elements for parallel computing	2	N/A
11	$meshI$	Mesh number in X direction	60	N/A
12	$meshJ$	Mesh number in Y direction	20	N/A
13	$meshK$	Mesh number in Z direction	20	N/A
14	L_I	Length in X direction	20	km
15	L_J	Length in Y direction	20	km
16	L_K	Length in Z direction	20	km
17	ρ	Density	3000	kg/m ³
18	λ	Lamé's constant	30	Gpa
19	μ	Shear modulus	30	Gpa
20	$refvisc$	Reference viscosity	0.125e-17	Pa ⁻ⁿ /s
21	$activationE$	Activation Energy	276.0e+3	kJ/mol
22	vis_{min}	viscosity minimum cutoff	1.0e+18	Pa * s
23	vis_{max}	viscosity maximum cutoff	1.0e+27	Pa * s
24	$srexponent$	Power of power law in viscosity	3.05	N/A
25	$\varepsilon_{p_i}^1$	initial plastic strain for piecewise Type one weakening	0	N/A
26	$\varepsilon_{p_i}^2$	initial plastic strain for piecewise Type two weakening	0	N/A
27	$\varepsilon_{p_e}^1$	end plastic strain for piecewise Type one weakening	0.1	N/A
28	$\varepsilon_{p_e}^2$	end plastic strain for piecewise Type two weakening	0.33	N/A
29	C_i	initial Cohesion for piecewise weakening	44	Mpa
30	C_e	end Cohesion for piecewise weakening	4	Mpa
31	ϕ	Friction angle	30	°
32	$remesh_{timestep}$	Remesh when timestep reach its value	400000	N/A
33	$remesh_{length}$	Remesh when ratio between current global minimum of the ratio of a tetrahedrons volume to one of its surface area to its initial value	0.6	N/A
34	$topTemp$	Surface temperature	0	°C
35	$bottomTemp$	Bottom temperature	1300	°C
36	V_x	Half spreading rate	7.9e-10	m/s

Table 1: Summary of 3D Model Parameters

3 3D Results

XT: add one more section as an individual file/chapter for 2D models description. Currently, we have three factors controlling the model behaviors. They are three ranges of M variation along the ridge axis ($0.5\sim0.7$; $0.5\sim0.8$; $0.2\sim0.8$), three functional forms of M variation (linear; sinusoidal; square root) and two types of weakening rate (Type one and Type two) as described in detail in the section “Parameters to control”.

In this “Results” chapter, we will first describe in detail the model behaviors of two reference models. Then, we will compare the reference model and the other data points with different setup parameters.

3.1 Reference models

We consider two models as our reference models: one, M varies linearly from 0.2 to 0.8 along the ridge axis with increasing Z; two, constant M along the ridge axis as a comparison to the changing M models.

3.1.1 M varies along the ridge-axis (M28LinT1 Table 2)

As shown in Figure 8, the model creates a median valley that both widens and deepens through time and the rate of its widening and deepening at a specific location (in terms of Z-axis) is inverse proportional to the rate of local magma supply (i.e. M value). OCCs with more than one kilometer in relief and tens of kilometers in wavelength are produced in the model. One interesting behavior worth noting is that corrugations with hundred-to-kilometer wavelengths are also produced by the model.

As shown in Figure 8.a, in the first 7.5kyr, high angle ($\sim 60^\circ$)(consistent with Anderson’s theory of faulting mechanics for a frictional angle of 30°) normal faults (shown as higher plastic strain shear bands with a thickness of $2\sim4$ times of the width of a single hexahedron element) begin to form near the ridge axis in terms of plastic strain localization

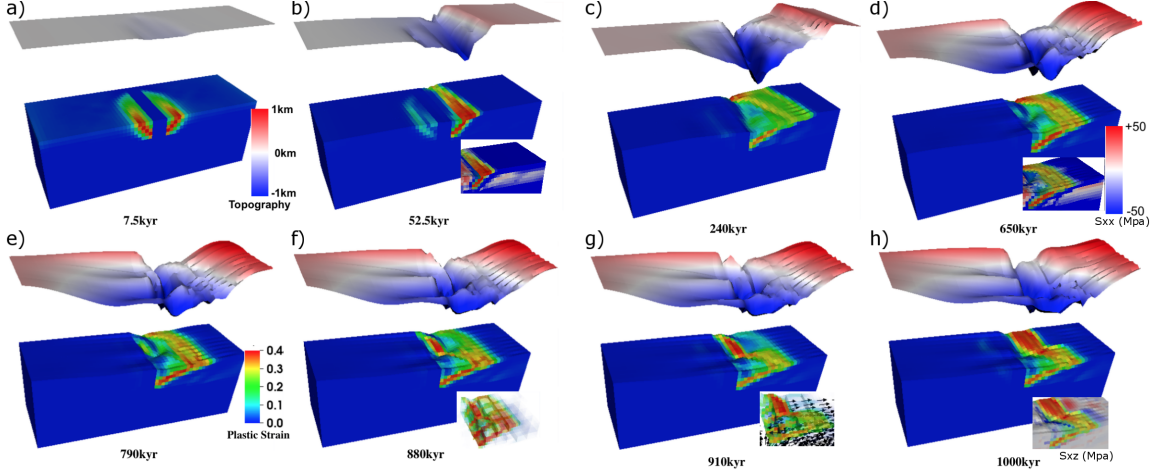


Figure 8: Reference model one: M linearly increases from 0.2 to 0.8 from front to back, Type one weakening (M28LinT1) (Table 2). The top layer is the topography of the model with five times vertical exaggeration. The color scale within Figure 8.a is for the topography. Initial seafloor is marked as a reference of zero km in height. The green, yellow and red colors in the background of blue model domain are plastic strain. Its color scale is shown in Figure 8.e. The number with kyr as a unit beneath each model result is the time for the model with a unit of thousands of year. The two insets in Figure 8.b and Figure 8.d is for stress σ_{xx} (S_{xx} in the figure). Positive value (pink and red) means tension and negative (blue) is compression. The inset in Figure 8.h is for shear stress σ_{xz} (S_{xz} in the figure). It share the same color scale with insets in the Figure 8.b and Figure 8.d. The inset in Figure 8.f is a transparent view of plastic strain. The inset in Figure 8.g shows both plastic strain and the velocity vector. Indicated by the velocity vector, the hanging wall of the detachment fault at low M region (M 0.2~ M 0.5) is moving in an opposite direction to the hanging wall at higher M region (M > 0.5).

near the ridge center (weakest place to initiate a fault), because of the thickness of the crust is thinnest at the ridge center due to our thermal structure setup. For each timestep, the tensional stress accumulates faster at the lower M side where the crust reaches a yielding point earlier than higher M side and so the fault first initiate at the front (lower M side) and then propagates to the back (higher M side). However, the along ridge-axis coupling (internal strength preventing relative displacement (i.e. rotation, offset) between two neighbors along the Z-axis) assists in fault propagation from front to back and reduces the time difference in initiation of faulting along the ridge-axis ~~when comparing with separate 2D models~~ [It probably will be verified after a 2D results analysis and conclusion].

At 52.5kyr (Figure 8.b), the normal fault on the right hand side of the ridge axis con-

tinues to evolve while the one on the left becomes inactive. The choice of which fault will develop is a random event since the model setup is symmetrical across the ridge-axis. The timing difference of initiation of faulting along the ridge axis creates an offset in X-axis direction between along ridge-axis breakways that the breakaway at the lower M side extends further than that of the higher M side (Figure 25). This offset remains constantly around three elements until time 295kyr (Figure 25.d) because the extending velocity of the breakaway to move away from the ridge-axis is only controlled by the far field extension rate, V_x . XT:Why after 295kyr the offset reduces needs to be answered. I don't know now.

Probably partly due to healing that earlier the fault initiation, more healing it experiences.

In addition, as shown in the inset of (Figure 8.b) with status of σ_{xx} distribution, as the fault offsets, crust at the footwall begins to bend in a clockwise rotation (view from front) (Figure 28) and the neutral plane ($\sigma_{xx} = 0$) is shown as the boundary between blue (compression) and pink (tension). In the “Discussion” section, we will show that this bending force created in the crust of footwall together with fault weakening as a trade-off factor is essential for faulting evolution. XT:Delete this add after finish discussing the bending force and weakening effect.

At 240kyr (Figure 8.c), the median valley further deepens and widens. The detachment keeps active and extends to $\sim 18\text{km}$ in length horizontally (longest at $M= 0.2$) with the dip angle decreases from initially $\sim 60^\circ$ to 30° (at the root of the fault) and 0° where the fault interface is exposed to the seafloor. However, for the detachment at the higher M side (especially the last three elements along the Z-axis), the dip angle remains high. The maximum relief between highest point in breakaway and lowest point in the median valley becomes larger than 1km. Corrugations show up at the lower M side, at the front tip of the extending fault interface. The lowest topography points inside the median valley evolves from a straight line parallel to the ridge-axis (Figure 25.a) to a line oblique to the ridge-axis (Figure 25.b,c,d).

At 650kyr (Figure 8.d), the median valley continues to deepen and widen. The break-

aways along the ridge-axis already ~~XT~~moved out of the model domain [it should not, if breakaway move with 25km/yr(half spreading rate), since the distance between initial break (5km away from ridge center) and right wall of the model domain is about 25km which needs 1Myr to reach. But now is only 650kyr. Why is it?]. The fault offset is already larger than the thickness of the crust and the upper mantle materials begin to be exhumed to the surface. The previous fault interface bend over to a negative dip angle (dip in an opposite direction) and produces a dome shape OCC with corrugations on its surface parallel to the spreading direction. The previous lowest topography points evolve to a curve with bigger curvature. Compared to the inset in Figure 8.b, the total length of the bending crust decreases. A hint of a near-axis secondary fault begin to initiate at the high M side ($10 < Z < 15$) as a form of tensile failure. ~~XT~~Its formation will be discussed in Discussion section accompanied by the stress status analysis.

At 790kyr (Figure 8.e), the initial tensile failure immediately ajacent to the ridge center (hint of the secondary fault) begin to evolve and propagate to higher Z region.

At 880kyr (Figure 8.f), at the higher M side, the initial tensile failure evolves to a high angle near-axis secondary normal fault and replace the initial detachment as indicated in the inset of transparent view of plastic strain.

At 910kyr (Figure 8.g), the secondary normal fault results in a strong constrast in moving directions between high M side and low M side near the ridge-axis that at the high M side, previous hanging wall becomes footwall and moves with spreading direction on the right, however, at the low M side, due to deficit in magma supply, the hanging wall is coupled with conjugate plate and moves to the left as shown in the inset. This opposite direction motion creates a strong shear stress region $\sim 45^\circ$ oblique to the ridge-axis (inset of Figure 8.h) and produces new lowest topography points align with it. Combined with previous lowest topography points, an “X” shape topography low is created.

Corrugations are observed in the model since 240kyr. It will be further discussed in the discussion chapter.

3.1.2 Constant M along the ridge-axis

XT: This section needs to be revised and add more details into the model description. Another reference model is the model with constant $M = 0.8$ along the ridge axis as a comparison to the changing M models.

As shown in Figure 9, this constant M along the ridge-axis model creates a median valley of $\sim 20\text{km}$ in width and $1 \sim 2\text{km}$ in depth which is similar to generally observation of Mid-Atlantic Ridges. The width and depth of the median valley is almost constant along the ridge-axis. The variation along the ridge-axis in breakaway and termination as well as the existence of corrugation mentioned in reference model one are not observed.

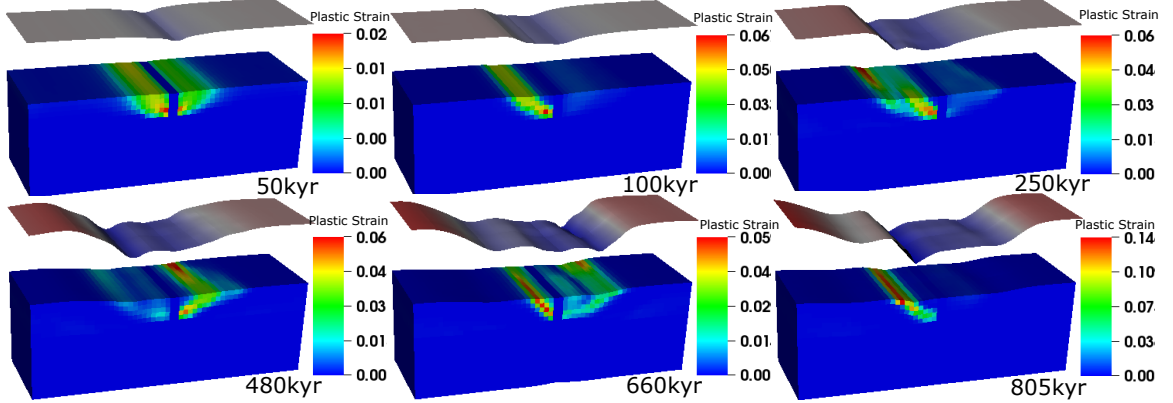


Figure 9: M88ConT2 (Table 2). Reference model two: constant $M = 0.8$ along the ridge-axis (i.e. Z axis). Type two weakening.

Based on the previous experience in pseudo-2D models or [Lavier et al., 2000], with higher characteristic fault offset (ΔX_c) for Type two weakening compared with Type one weakening, the frequency of normal faulting alternation is higher for $M > 0.5$ cases. However, interesting enough, when comparing pseudo-2D and 3D models when they are using Type two weakening under case of $M = 0.8$, even though the 3D Model has a larger ΔX_c of 1km than that of pseudo-2D model of 0.5km, 3D model has a lower frequency of faulting alternation. Since M is constant 0.8 along the ridge-axis, the effect of along ridge coupling that resists alternation need not be considered. One possibility is that the resisting bending force increase in a higher rate than linear with respect to increasing the length of

the ridge segment (Z_{max} km).

3.2 Tables of all the data points

Model	M range	Functional Form	Type of weakening	For short
1	M28	Linear	Type one	M28LinT1
2	M28	Sinusoidal	Type one	M28SinT1
3	M28	Square Root	Type one	M28SqrtT1
4	M57	Linear	Type one	M57LinT1
5	M57	Sinusoidal	Type one	M57SinT1
6	M57	Sinusoidal	Type two	M57SinT2
7	M57	Square Root	Type two	M57SqrtT2
8	M58	Sinusoidal	Type one	M58SinT1
9	M58	Sinusoidal	Type two	M58SinT2
10	M58	Square Root	Type one	M58SqrtT1
11	M58	Square Root	Type two	M58SqrtT2
12	M88	Constant	Type two	M88ConT2

Table 2: List of 3D numerical experiments. M28LinT1 and M88ConT2 are the two reference models.

Currently, we have run ~~XT~~hundreds of [find out exactly number that will be used in 2D model results conclusion] Pseduo-2D models for initial setup and benchmarking with previous studies (e.g. [Buck et al., 2005] and [Tucholke et al., 2008]). Based on those Pseudo-2D models, we further ran 11+1 (11 models with M variation along the ridge-axis and 1 model with constant M= 0.8 along the ridge-axis) 3D models shown in Table 2. The available data points are limited due to the huge computation expenses for 3D models (For each model to be run to 2Myr, usually needs 192 cores for about 2 days (around 10000 SUs). ~~XT~~use 96 cores can improve the efficiency a little bit (Longer time but smaller amount of SUs needed.)

Based on the available data points as shown in the tables, we are able to fix other parameters and only compare the model results with respect to: 1) Variation of the functional form; 2) Influence of weakening rate; 3) Variation of the range of M.

3.3 Variation of the functional form

How magma supply varies along the MORs ridge-axis remains a current research question and we do not have direct quantitative observation over it. However, from indirect geo-physical studies (e.g. gravity, seismology), people suggest a general qualitative pattern of 20 to 50 km long second-order ridge segment with magma mostly supply at the segment center and decreases to the end [Carbotte et al., 2015]. Since we do not know exactly how magma supply varies along the ridge, we try three functional forms (linear, sinusoidal and square root) for its variation along the ridge-axis.

3.3.1 Comparing M28 in terms of linear, sinusoidal and square root

As shown in the tables, M28 with Type one weakening is the only M range that has three functional forms data points available. There are two phenomena that show distinct differences with respect to different functional forms. One is the geometry and timing of the secondary fault. The other is the “Cut back” behavior mostly observed in the square root model.

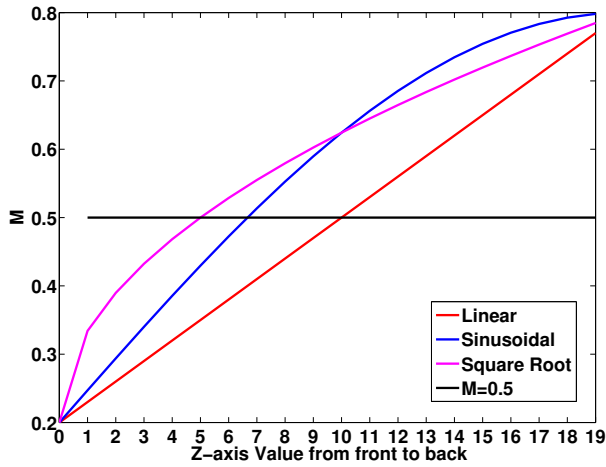


Figure 10: Three functional forms of M variation comparison. They begin to exceed the $M = 0.5$ black line at $Z=10, 7, 5$ for linear, sinusoidal and square root respectively.

Secondary Fault For linear, the secondary fault at higher M side begins to take place at around 900kyrs (Figure 11), its spatial distribution is at $M > 0.5$ region. It nucleates from the shear low (ridge center where $M = 0.5$) to the $M = 0.8$ end (Figure 10 where the red line begin to exceeds 0.5 at $Z = 10$). As it evolve, the initial detachment becomes inactive. This secondary fault creates another dome with initial composition likely to be volcanic rather than ultramafic, however, as it evolves, if it can last long enough to cut through the whole crust, mantle materials might exhumed to the surface. The composition of the domes observed at Kane magamullions is similar to this mechanism between ultramafic babel dome and eastern to it the crustal inside-corner high.

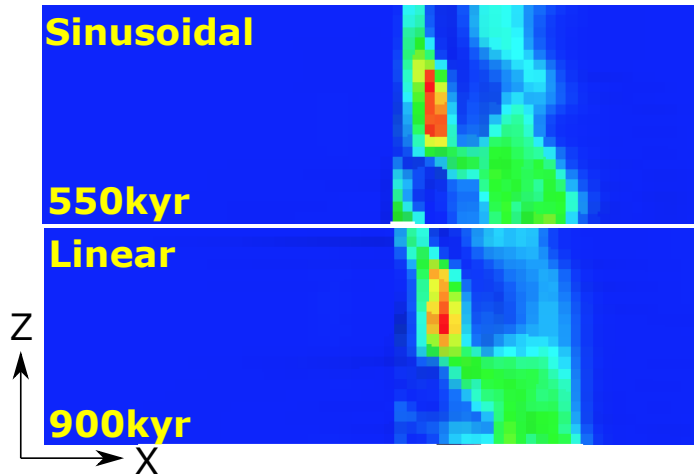


Figure 11: M28LinT1 versus M28SinT1 (Table 2). Secondary fault length comparison between linear and sinusoidal. Around 13 elements in length for sinusoidal compared to 11 elements for linear.

For sinusoidal, the secondary fault begins to form at a much earlier time around 550kyrs (Figure 11), this is due to the total area of $M > 0.5$ for sinusoidal functional form is higher than that of linear. Qualitatively, the total force to push the hanging wall of the detachment away from the dike for sinusoidal is larger than that of linear. The larger the force, the faster the detachment moves off axis, the earlier the secondary fault will appear. In addition, the total length of the secondary fault is longer due to the total length of M that is above 0.5 is bigger than that of the linear model (Figure 10). For square root, there is no secondary fault forming because the “cut back” behavior releases the tensional stress in the hanging

wall.

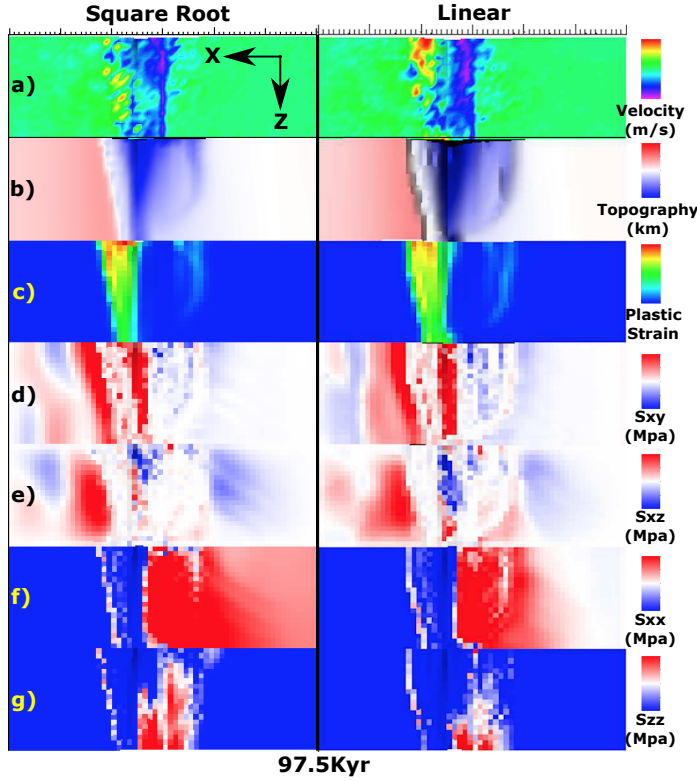


Figure 12: M28LinT1 versus M28SqrtT1 (Table 2) at 97kyr. View from top of the model.

Cut back The Cut back mostly happens in Square root functional form models. As shown in Figure 12, Figure 13 and Figure 26, between 97.5kyr and 100kyr, there are a cut backs in the square root model M28SqrtT1 at the low M side where hanging walls with surface area of $\sim 60 \text{ km}^2$ and $\sim 120 \text{ km}^2$ (the red block) suddenly rebound backwards towards the ridge-axis as seen in 100kyr and 160kyr (Figure 13.a and Figure 26.d,e,f), along with sudden topography drop (Figure 26.d,e 2nd row), σ_{xy} and σ_{xz} released, termination falls back (Figure 26.f 3rd row).

3.4 Influence of weakening rate

According to our available twelve 3D models, we have three pairs of models that both have Type one and Type two weakening while the range of M and functional form are maintained

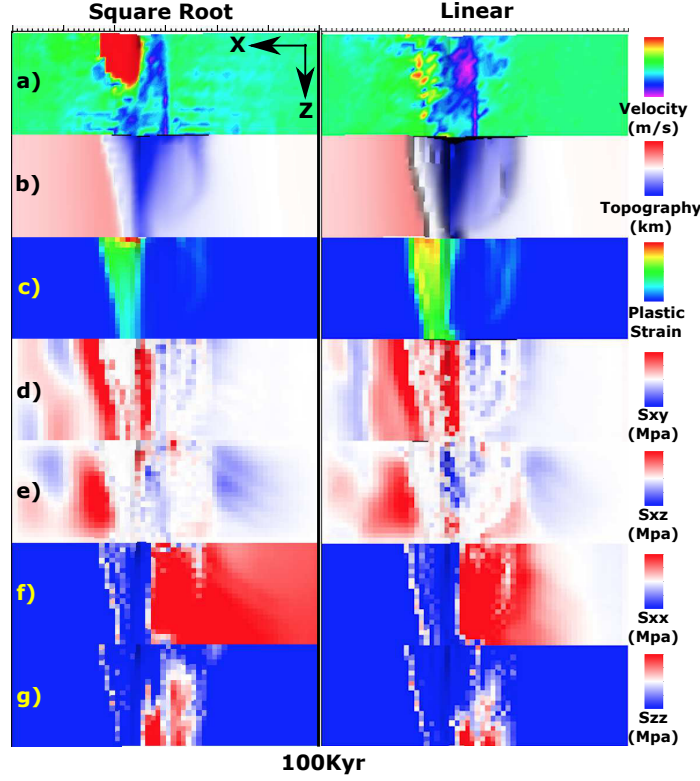


Figure 13: M28LinT1 versus M28SqrtT1 (Table 2) at 100kyr. View from top of the model.

to be the same. They are M57(sinusoidal), M58(sinusoidal) and M58(square root). We will describe their differences respectively.

3.4.1 M57SinT1 versus M57SinT2

There are very distinct differences between the two models. They share same functional form (sinusoidal) as well as M range (M57).

Initially, both models develop normal fault deformations on both sides of the ridge-axis at the low M side. The time for the faults to propagate toward the high M side and cut through the whole crust for M57SinT1 (25kyr) is one half of that for M57SinT2 (50kyr). At around 310kyr, a near axis secondary fault begin to evolve for M57SinT2 at higher M side ($Z > 5$) and soon take the place of initial fault, while at lower M side ($Z \leq 5$), the initial fault remains (Figure 14.a) and b)). However, for M57SinT1, cut back happens around 260kyr and help to maintain a high angle fault with closer to ridge-axis termination.

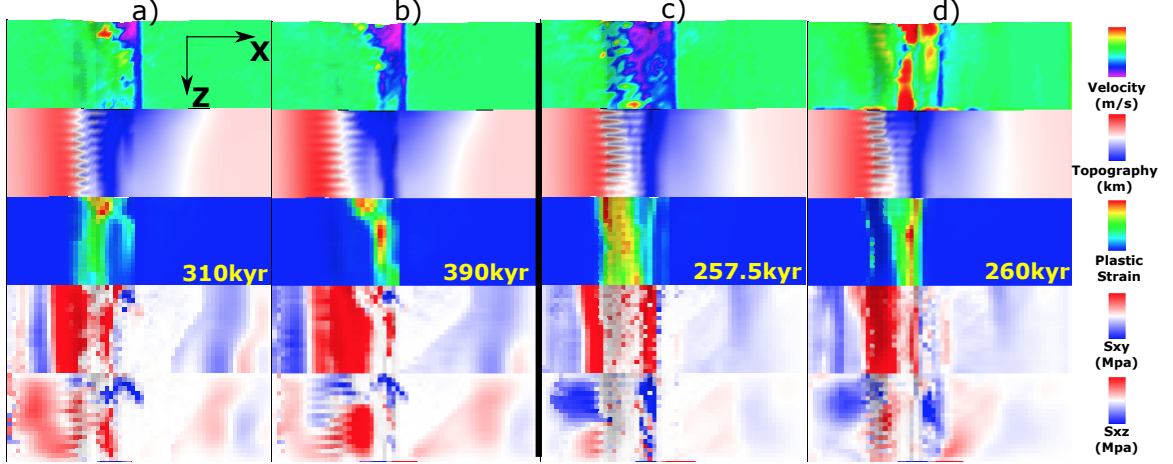


Figure 14: M57SinT2 versus M57SinT1 (Table 2). a) and b) are for M57SinT2, c) and d) are for M57SinT1.

The initial fault remains, no secondary fault forming (Figure 14.a) and b)). In addition, the width of median valley at low M side is wider for M57SinT2 than M57SinT1 (Figure 14.a) and b) versus c) and d)) due to slower weakening (Type two) allows a more distributed tensional stress σ_{xx} rather than fast weakening that once a fault is established, larger amount of tensional stress σ_{xx} will be released at the fault.

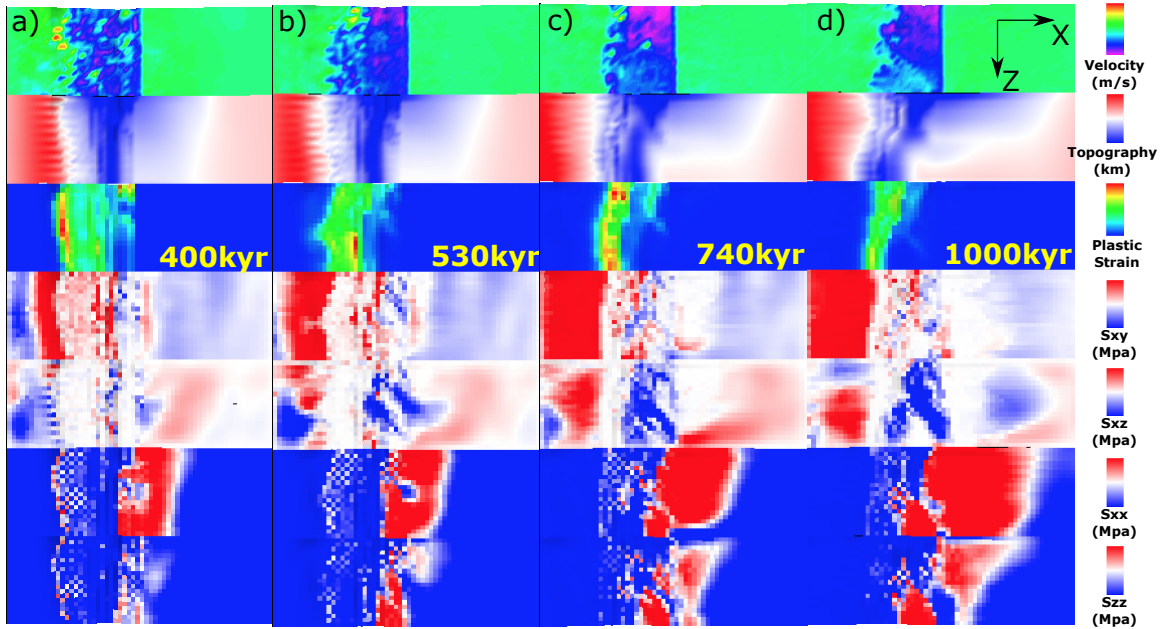


Figure 15: M57SinT1 (Table 2) faulting and stress evolution with respect to time.

M57SinT1 For M57SinT1, as shown in Figure 15, at 400kyr (Figure 15.a), there is a antithetic fault forming at the low M side accommodating part of the extension, which results in a curved termination at the far frontier. As it evolve (530kyr (Figure 15.b)), the termination at the low M side further recedes backward while the termination at the center ($Z = 11 \sim 13$) extends further. This curved termination leads to a curved topography (white curve in the second row). As the fault evolves and bends further away from the axis, at the time of 740kyr, another antithetic fault forming again at the low M side (Figure 15.c). It doesn't take the place of initial fault and disappear soon, however, it again releases tensional stress and results in that the termination at far front recedes backward. At 1000kyr (Figure 15.d), an Atlantiss Massif shape OCC is produced (low M side (lower magma supply) has a wider dome and high M side (higher magma supply) has a narrower dome) due to the along ridge-axis termination evolution. Corrugations with wavelength varying from hundreds to kilometers are also created.

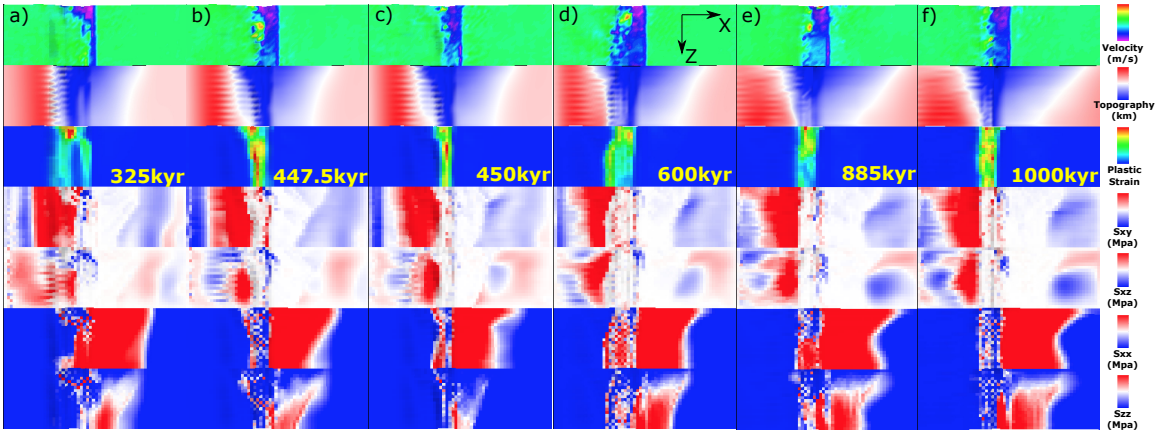


Figure 16: M57SinT2 (Table 2) faulting and stress evolution with respect to time.

M57SinT2 For M57SinT2, as shown in Figure 16, instead of maintaining one fault all the time for M57SinT1, it creates secondary fault at high M side with different mechanism several times. A secondary fault is created at 325kyr (Figure 16.a), when a new near axis normal fault take the place of the initial one at high M side. Between 447.5kyr (Figure 16.b) and 450kyr (Figure 16.c), termination falls back, and as it evolve, termination at the high

M side extends further at 600kyr (Figure 16.d). At 885kyr (Figure 16.e), a secondary fault propagates from low Z to high Z and terminates the further extended fault at high Z and maintain a near ridge-axis termination.

3.4.2 M58SinT1 versus M58SinT2

A major difference between M58SinT1 and M58SinT2 is that M58SinT1 keep faulting at one side of the ridge-axis while M58SinT2's fault alternates.

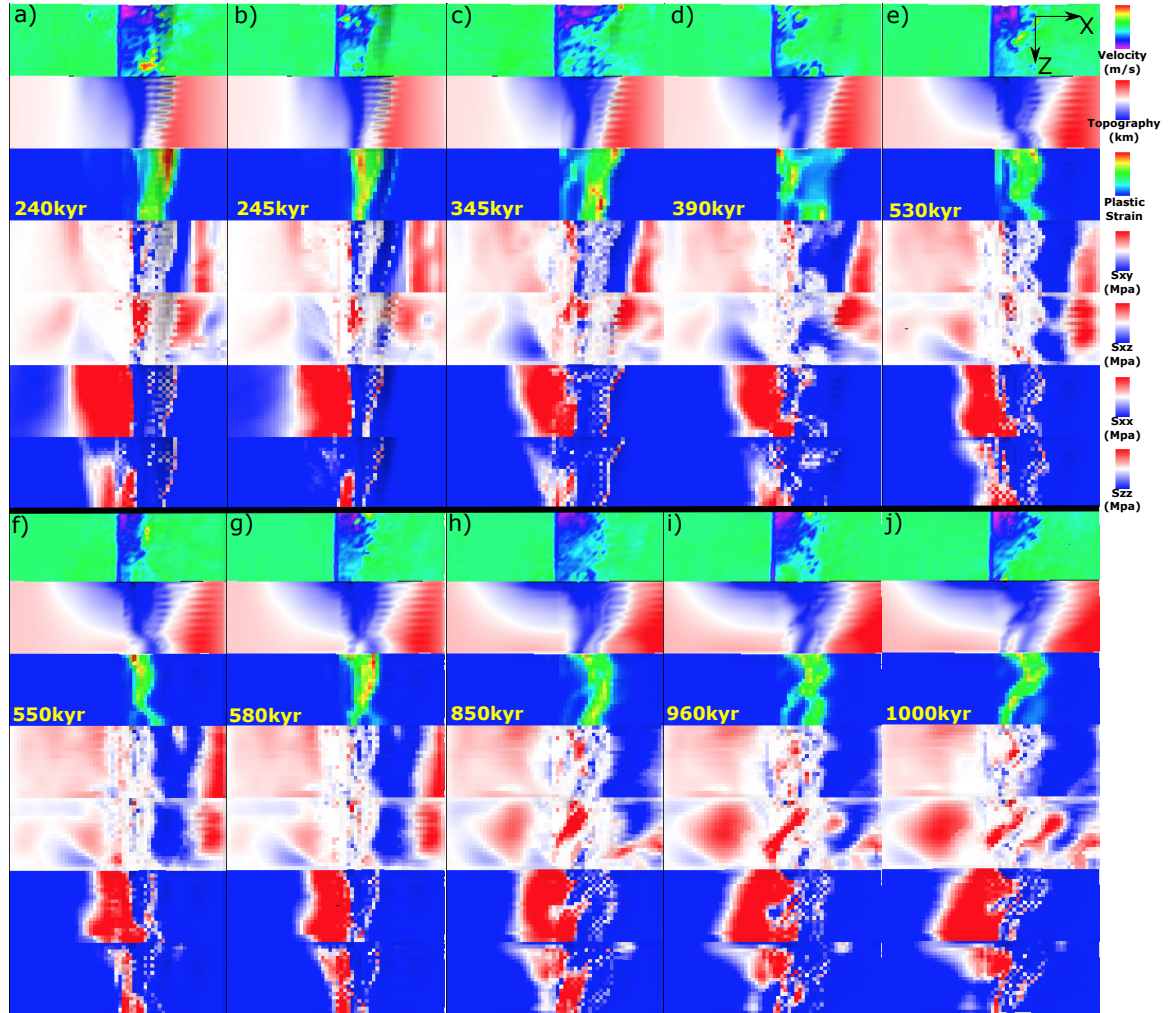


Figure 17: M58SinT1 (Table 2) faulting and stress evolution with respect to time.

M58SinT1 As shown in Figure 17, in 1Myr, the fault keeps on the right hand side of the ridge-axis. It evolves dynamically. Between 240kyr (Figure 17.a) and 245kyr (Fig-

ure 17.b), there is a cut back. At 345kyr (Figure 17.c), at low Z side, there are two offsetted antithetic faults ($Z=1 \sim 2$ and $Z=5 \sim 9$) in the hanging wall begin to evolve and soon connect to each other forming anastomosing fault zone. At 390kyr (Figure 17.d), the new near axis anastomosing fault zone replace the old further away from ridge-axis detachment. There is dextral σ_{xz} forming on the right hand side of the new anastomosing fault zone ((Figure 17.d), row 5) due to the offset between the new near axis fault at low Z side and extended further fault at high Z side and leads to the development of a $\sim 45^\circ$ shear zone connection between the new near axis fault zone at low Z side and the further away from axis original detachment at high Z side. It also creates a curved termination which will lead to a curved topography (boundary between blue and white) seen at 530kyr (Figure 17.e). Note that this curved termination can be a mechanism for producing large wavelength (several kilometers) undulating corrugations. Between 530kyr (Figure 17.e) and 550kyr (Figure 17.f), there is another cut back happens. Terminations fall backwards to near ridge-axis position. At 580kyr (Figure 17.g), at the high Z side, a new near ridge-axis high angle normal fault begin to initiate under the assistance of rotational force from low Z side due to along ridge-axis coupling. This produces a large rider block with several kilometers in its length scale. Previous “S” curved termination now evolves to a half circle curve and it soon affects the curve of topography as seen at 850kyr (Figure 17.h). Due to along ridge-axis variation in diking, a large sinistral shear zone (red region $\sim 40^\circ$ oblique to ridge axis seen in 5th row of 960kyr (Figure 17.i)) keep developing and cut the circle curved fault zone at 850kyr (Figure 17.h) into a new fault zone with higher curvature as seen in 1000kyr (Figure 17.j).

M58SinT2 As shown in Figure 18, the fault initiates on the left hand side of the ridge-axis (Figure 18.a). Low Z side extends further than high Z side. It takes around 100kyr to form into a localized fault plane due to slower rate of weakening. At 215kyr (Figure 18.b), another fault on the conjugate plate begin to evolve and replaces the initial one. As seen from

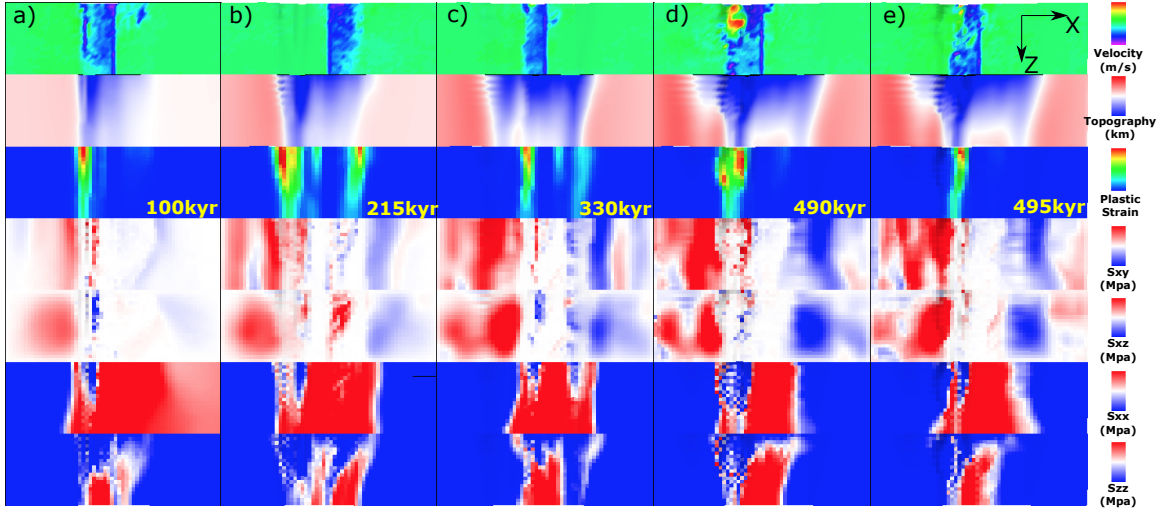


Figure 18: M58SinT2 (Table 2) faulting and stress evolution with respect to time.

(Figure 18.b), corrugations are created at low Z side. At 330kyr, a third fault forming at the left hand side of the ridge-axis. Between 490kyr (Figure 18.d) and 495kyr (Figure 18.e), there is a cut back.

3.4.3 M58SqrtT1 versus M58SqrtT2

The major difference between M58SqrtT1 and M58SqrtT2 is also whether the normal fault alternates or not.

M58SqrtT1 As shown in Figure 19, initially, there is a 5 element offset between breakaways along the ridge-axis due to along ridge-axis variation in diking (Figure 19.a). At 370kyr (Figure 19.b), there is a vertical tensile failure at $Z= 1 \sim 2$. Two parallel dextral (blue) shear regions are seen (5th row). The low Z shear zone assists in the shear failure observed at 400kyr (Figure 19.c), and it develops into near ridge-axis normal fault ($Z=4 \sim 12$) and propagates to high Z side which eventually cuts through and reaches $Z= 20$ and replaces the initial extended fault at high Z side at 460kyr (Figure 19.d). The vertical tensile failure zone at $Z= 1 \sim 3$ (Figure 19.d 3rd row) begin to evolve and assists in the initiation of a new near ridge-axis high angle normal fault which connect with the fault at the high Z side (Figure 19.e) at 590kyr. At 660kyr (Figure 19.f 3rd row), there is a hint of high angle

normal faulting at $Z= 1 \sim 3$ of conjugate plate. But it doesn't develop. At 730kyr (Figure 19.g 5th row), a dextral (blue) shear zone at the low Z side help to create the faulting pattern seen at 780kyr (Figure 19.h 3rd row), a concave termination with a wavelength of 10 kilometers and it has the potential to create a large wavelength corrugation. Meanwhile, at the low Z side, near the ridge-axis, there is a antithetic fault forming at the hanging wall of the detachment and it later propagates to high Z side (Figure 19.i). From 820kyr to 880kyr, the antithetic fault evolves to near ridge-axis normal fault and connects with the detachment at the high Z side (Figure 19.j). In addition, a tensile failure shows its hint at the low Z side ($Z= 1 \sim 5$) of the conjugate plate.

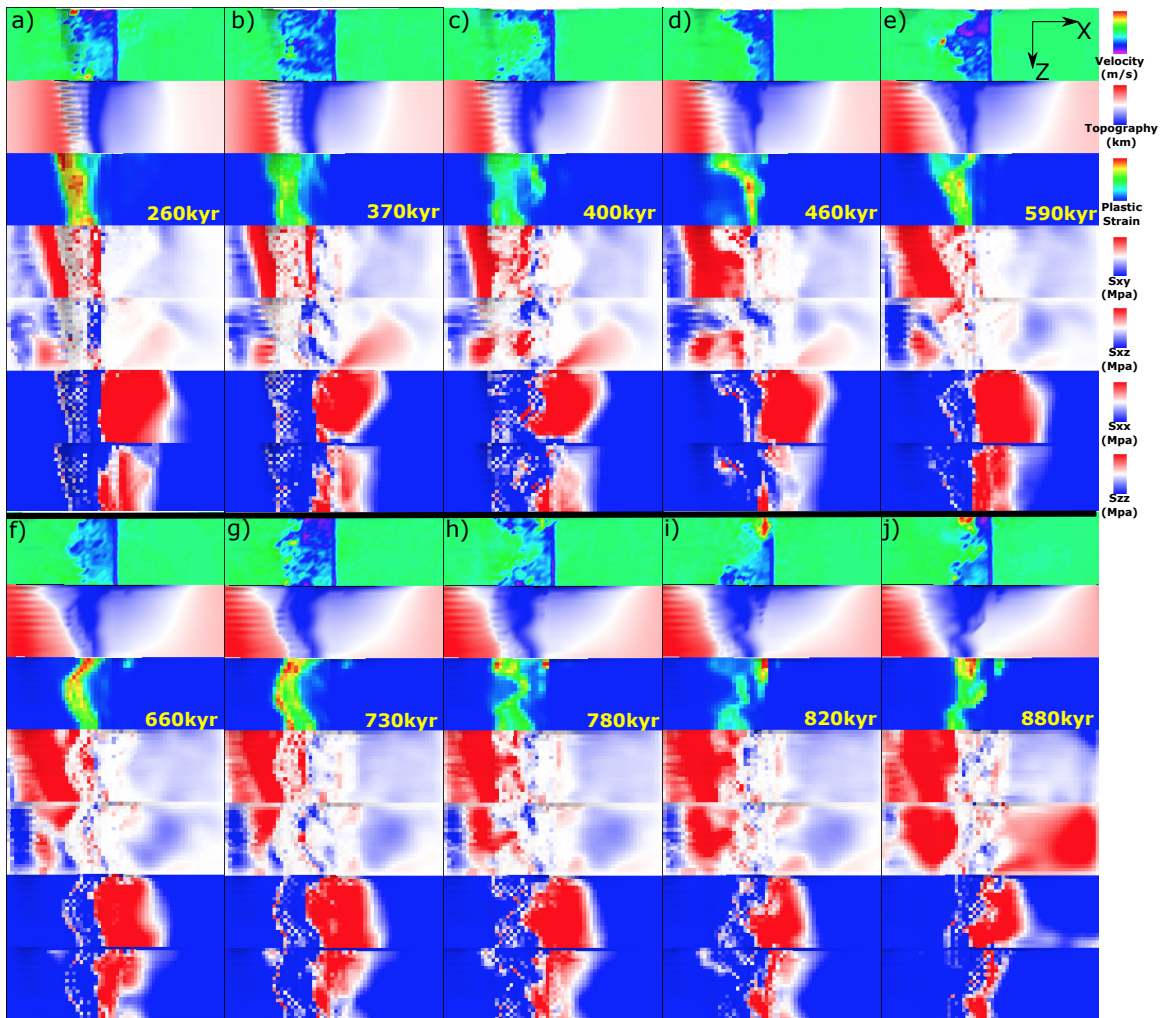


Figure 19: M58SqrtT1 (Table 2) faulting and stress evolution with respect to time.

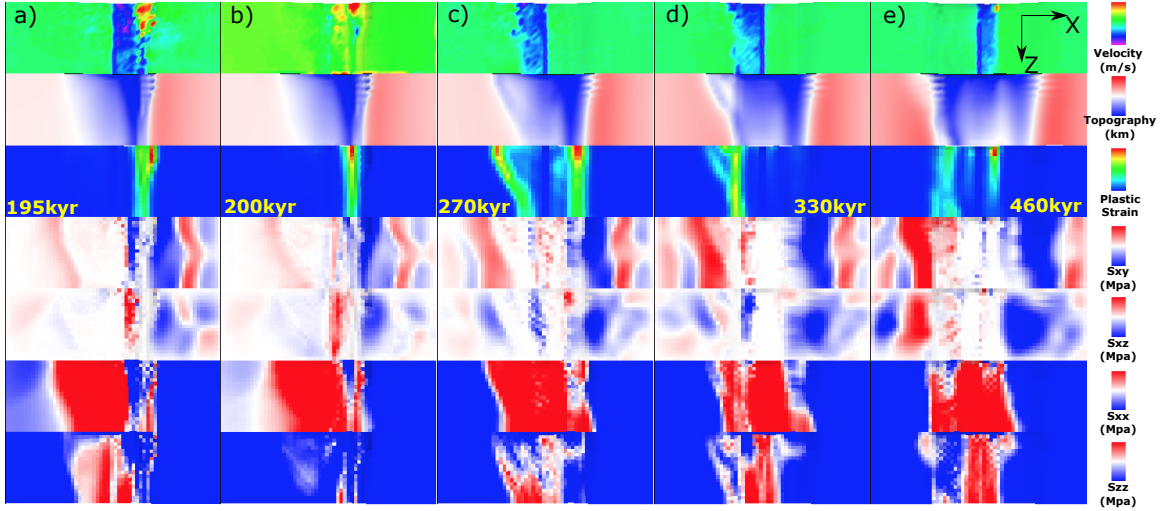


Figure 20: M58SqrtT2 (Table 2) faulting and stress evolution with respect to time.

M58SqrtT2 As shown in Figure 20, at 195kyr (Figure 20.a), due to transtensional stress at low Z side ($Z = 1 \sim 6$), several corrugations begin to evolve. At conjugate plate, dipping toward axis shear zone σ_{xy} (red at 4th row) show its curve and keeps accumulating. σ_{xx} is also accummulating on the conjugate plate. Between 195kyr (Figure 20.a) and 200kyr (Figure 20.b), there is a cut back. At 270kyr (Figure 20.c), immediately above and following the curved shape shear σ_{xy} zone on the left hand side of the ridge-axis, a new fault begin to evolve and replace the initial fault on the right. At 330kyr (Figure 20.d), at the low Z side, a new near axis high angle normal fault take the place of initial further away from ridge-axis fault partly due to rotational force from along ridge coupling. At 460kyr (Figure 20.e), another normal fault begin to evolve on the right hand side of the ridge-axis.

3.5 Variation of the range of M

So far, we have three ranges for M variations along the ridge-axis (M28, M57 and M58) with same segment length of 20km. Among the 12 available models, two M58 models and the constant $M = 0.8$ model with Type two weakening produce fault alternation while others do not. Generally, M57 and M58 models create a median valley much narrower and shallower than that of M28 models. $\frac{dM}{dz}$ is larger for M28 than M58 and M57.

3.5.1 M28SinT1 versus M57SinT1 versus M58SinT1

M57SinT1 versus M58SinT1 For description of M57SinT1 evolution with respect to time, please refer to Section 3.4.1 and Figure 15. For description of M58SinT1 evolution with respect to time, please refer to Section 3.4.2 and Figure 17. Comparing M57SinT1 and M58SinT1, the major difference is that the faulting pattern evolution for M58SinT1 is much more dynamic with a higher frequency of secondary faults, cut back and offseted fault segments connection. For M58SinT1, the new secondary near ridge-axis normal or antithetic faults usually replace the existed one. However, for M57SinT1, diking is not strong enough to create big enough stress perturbation along the ridge-axis for secondary or antithetic faults to take the place of the original one. At the low Z side, near ridge-axis antithetic fault only helps to accommodate tensional stress which help maintain a high angle normal fault with near to ridge-axis termination while the termination at the high Z side gradually move off axis. This creates a OCC with larger dome at lower magma supply side than that of higher magma supply side which is opposite to the shape of OCC created by M58SinT1.

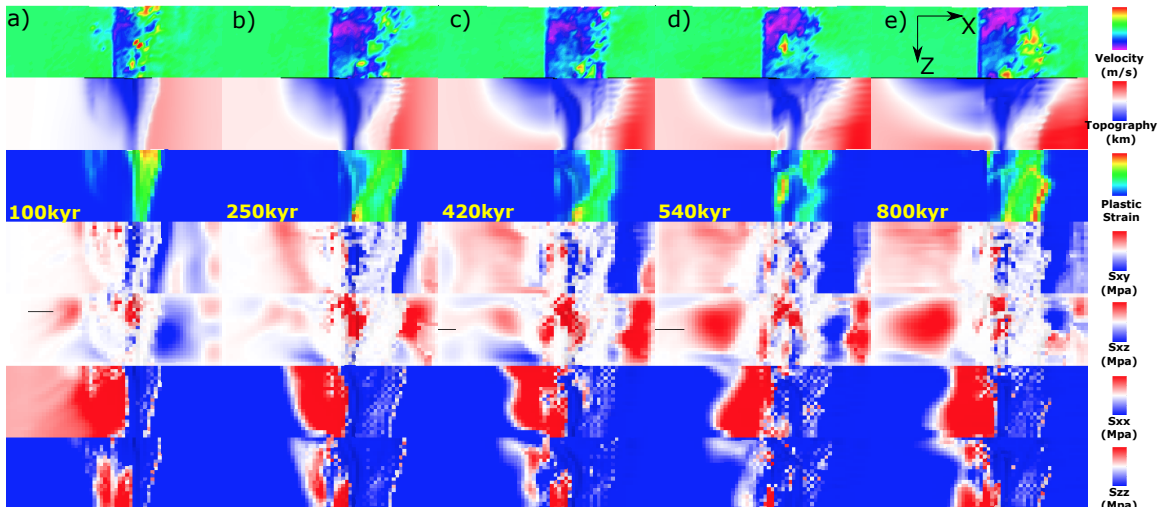


Figure 21: M28SinT1 (Table 2) faulting and stress evolution with respect to time.

M28SinT1 As shown in Figure 21, faulting evolution is much less dynamic than that of M58SinT1. Faulting keeps on the right hand side of the ridge-axis. Only one secondary fault is formed at around 540kyr (Figure 21.d). Initially, at 100kyr (Figure 21.a), at the low Z side, the normal shear zone at conjugate plate takes up part of the extension and leave a dent in the topography. But it doesn't last long. The initial breakaway of the detachment extends further away from ridge-axis with four elements in along ridge-axis offset at 250kyr (Figure 21.b). At 420kyr, at the high Z side, a hint of new near ridge-axis high angle normal fault begin to show up. It delvelop into a secondary fault at 540kyr (Figure 21.d) and propagates toward high Z side. This results in a sinistral shear zone (red region in 5th row). At the low Z side ($Z= 1 \sim 3$), a tensile failure can be seen and it take up part of the extension at the low Z side which results in the recede of termination at the low Z side as seen at 800kyr (Figure 21.e) while the termination at higher Z side extends further away from the ridge-axis.

3.5.2 M57SinT2 versus M58SinT2

For description of M57SinT2 evolution with respect to time, please refer to Section 3.4.1 and Figure 16. For description of M58SinT1 evolution with respect to time, please refer to Section 3.4.2 and Figure 18. A major difference is that M57SinT2 does not create alternating normal faults on each side of the ridge-axis while M58SinT2 does. *XT:Why this seemingly small change could lead to such a to the first order difference in model behaviors?*

3.5.3 M28LinT1 versus M57LinT1

For description of M28LinT1 evolution with respect to time, please refer to Section 3.1.1.

M57LinT1 As shown in Figure 22, between 160kyr (Figure 22.a) and 162.5kyr (Figure 22.b), there is a cut back. The corrugation is very severe and have a discrete distribution

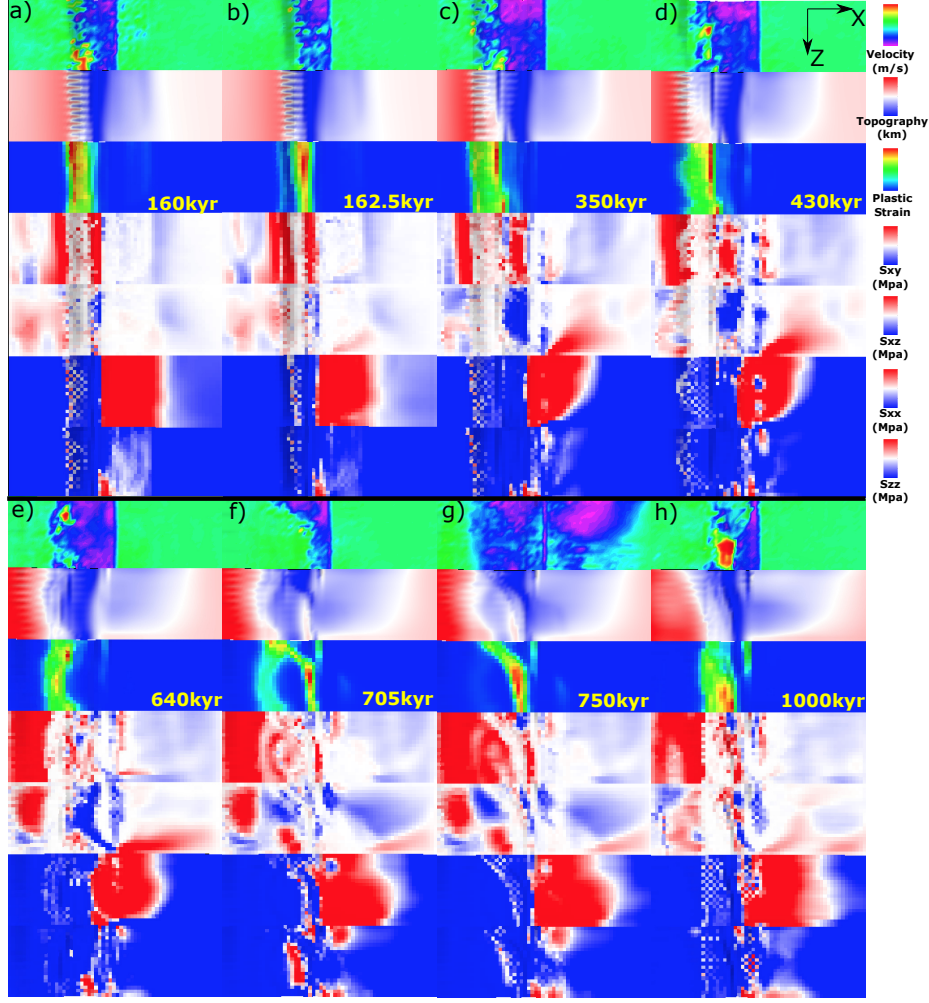


Figure 22: M57LinT1 (Table 2) faulting and stress evolution with respect to time.

with one element width as its wavelength. The frontier of breakaway also shows discrete distribution of σ_{xx} and σ_{zz} alternating between tension and compression which might be the reason for the undulating topography. At 350kyr (Figure 22.c 3rd row), the two offsetted red line indicates tensile failure at the termination and the shorter one at the high Z side helps maintain a near ridge-axis high angle normal fault. At 430kyr (Figure 22.d), the presence of vertical tensile failure near the ridge-axis at the low Z side is responsible for the recede of the front of the plastic strain at $Z= 1 \sim 3$. While at $Z=5 \sim 10$, the breakaway keeps extending further away from the ridge-axis. This curved front results in a curved topography as seen in 640kyr (Figure 22.e) and is also responsible for the large dextral shear (blue) zone (5th row). At 705kyr (Figure 22.f), a new near ridge-axis secondary fault begin

to evolve and replace the original one at high Z side with a length of ~ 15 kilometers. The secondary fault also connect with the further away from ridge-axis original fault at low Z side. The topography at 1000kyr (Figure 22.h) is a result of the curved and later connected fault. The frontier of the plastic strain at high Z side soon catch up with that at the low Z side due to the presence of a tensile failure zone at the low Z side that has taken up part of the extension.

3.5.4 M28SqrtT1 versus M58SqrtT1

For description of M28SqrtT1 evolution with respect to time, please refer to Paragraph 3.3.1 and Figure 30.

For description of M58SqrtT1 evolution with respect to time, please refer to Paragraph 3.4.3 and Figure 19.

3.5.5 M57SqrtT2 versus M58SqrtT2

For description of M58SqrtT2 evolution with respect to time, please refer to Paragraph 3.4.3 and Figure 20.

The major difference between M57SqrtT2 and M58SqrtT2 is that M57SqrtT2 keeps faulting at the same side of the ridge-axis while M58SqrtT2 alternates.

M57SqrtT2 For M57SqrtT2, there are totally six small scale cut back happen at 282.5kyr, 290kyr, 365kyr, 452.5kyr, 482.5kyr and 540kyr respectively (the model stops at 540kyr). As shown in Figure 23, the fault keeps on the left hand side of the ridge-axis. At 200kyr (Figure 23.b), a new near ridge-axis high angle normal fault begin to evolve and take the place of the initial one. As the fault evolve, a transient stage of discontinuous abyssal hill is produced at the low Z side as seen at 225kyr (Figure 23.c). The fault propagate toward high Z side and cut through the plate at ~ 245 kyr (Figure 23.d) when sawtooth shape topography at the low Z side (2nd row) is created by sawtooth shape σ_{xx} (6th row) and σ_{zz}

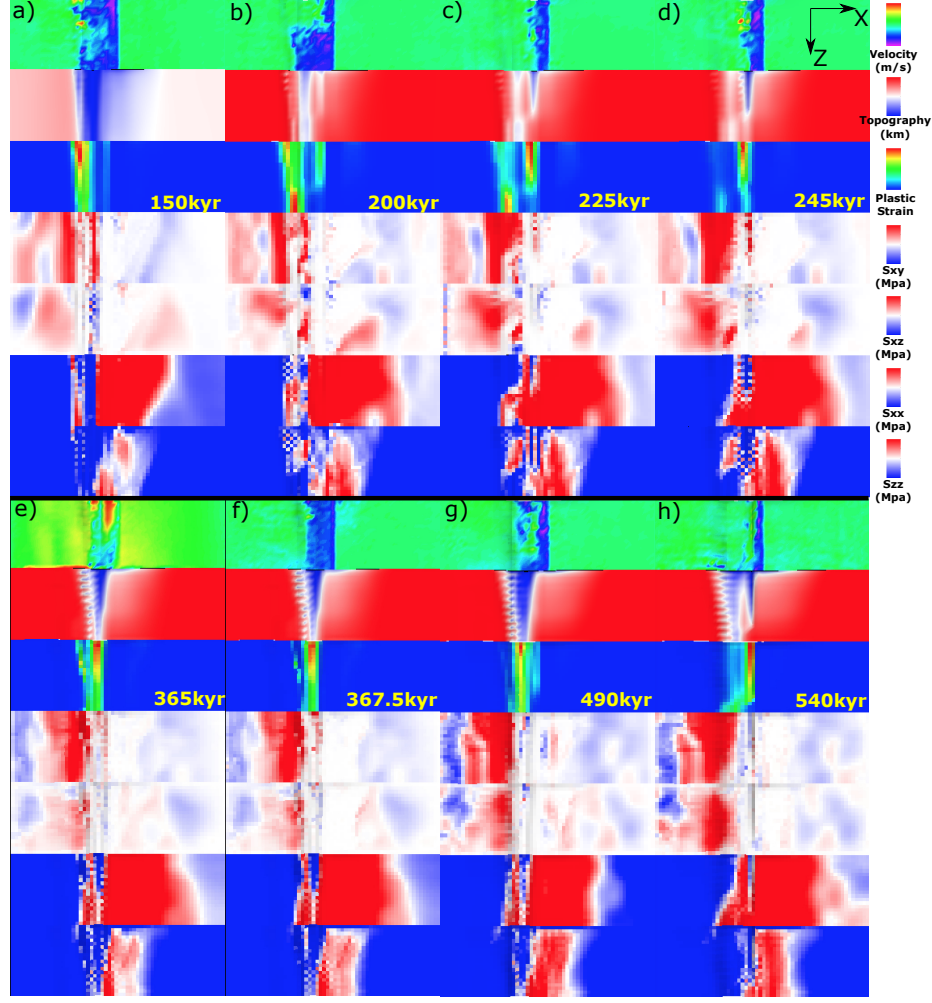


Figure 23: M57SqrtT2 (Table 2) faulting and stress evolution with respect to time.

(7th row). Between 365kyr (Figure 23.e) and 367.5kyr (Figure 23.f), there is a cut back. At 490kyr (Figure 23.g), there is new near ridge-axis antithetic fault on the hanging wall which terminates the old fault and develops into a vertical near ridge-axis tensile failure as seen at 540kyr (Figure 23.h).

3.6 Summary of Results

There are several behaviors that are controlled by the model parameters. Generally, only M58 models with Type two weakening produce alternating faults on both side of the ridge-axis. All the models show corrugations. As for faulting patterns in terms of evolution

frequency, usually Square root is more dynamic than Sinusoidal than Linear, M58 is more dynamic than M57 than M28.

Following tables are a summary of the model behaviors with respect to different setup parameters.

A	Alternating Fault	C	Corrugation	SL	Shear Topography Low
NA	Not Alternating	SF	Secondary Fault on one side	CB	Cut Back
DD	Double Dome	AM	Atlantis Massif Shape		

Table 3: Model behaviors in short.

Based on the 11 models with M variation, we observed eight first-order behaviors as shown in Table 3.

M range Type \	M28	M57	M58
Type one	NA; C; SL; SF _{1500kyr} ; DD	NA; C; SF _{1380kyr} ; CB _{330kyr} ; AM(opposite z)	
Type two			

Table 4: Linear functional form.

M range Type \	M28	M57	M58
Type one	NA; C; SL; SF _{995kyr}	NA; C; SL; SF _{760kyr;1320kyr} ; CB _{520kyr} ; AM	NA; C; SL; CB _{510kyr} ; SF _{760kyr;1140kyr;1990kyr}
Type two		NA; C; SL; SF _{680kyr} ; CB _{905kyr}	A _{450kyr;600kyr} ; C(only at low M); CB _{990kyr}

Table 5: Sinusoidal functional form.

M range Type \	M28	M57	M58
Type one	NA; C; SL; CB_{205kyr} ; CB_{330kyr} ; $CB_{1025kyr}$		NA; $C_{1770kyr}$ (due to shear with dif wave length); SF_{860kyr} (high M); $SF_{1190kyr}$ (low M)(Dog Bone); $SF_{1690kyr}$
Type two		NA; C; SF_{435kyr} ; $SF_{1060kyr}$; CB_{585kyr} ; CB_{735kyr} ; CB_{910kyr} ; CB_{970kyr}	A_{550kyr} ; $920kyr$; C; CB_{400kyr}

Table 6: Square root functional form.

4 Discussion

Generally, all models forms a median valley that deepens and widens toward the lower M side (Figure 8) except the reference model with constant $M = 0.8$ (Figure 9). The topography observed in our models, to the first order, is controlled by the spatial and temporal distributions of faulting and to the second order, results from elastically deformation (e.g. The gradual deepening and widening of the median valley; The bending of the crust at the footwall side of the detachment fault results in a domal shape of the fault interface as a mechanism for producing the dome shape of OCCs).

The pattern of the deformation (faulting and elastic deformation) is controlled by the evolving stress in the crust in terms of its distribution and magnitude. The stress evolution is a result of the interaction processes between tectonics and magmatism. Due to constant seafloor spreading, tensional stress orthogonal to the ridge-axis in the crust keeps accumulating. At the same time, along ridge-axis varying diking partially accommodates the stress from far field extension and perturbs the homogeneity state of stress distribution along the ridge-axis. Accumulated stress will be largely released when the tensile or shear failures establish.

Since the model behavior is very complicated. We will focus on the effects being brought by the along ridge-axis variation in diking. Thus, it is worth considering a thought experiment with two end members: One, the along ridge-axis coupling is rigid, so that even along ridge axis variation in M exist, once a fault determined to develop, it will cut through the whole model domain along the ridge-axis(Z-axis) simultaneously. The other end member is that there is totally no coupling along the ridge-axis. So that each slice of crossection profile across the ridge behave separately without being influenced by its neighbour to a extreme that the model behavior is just a combination of 20 pseudo-2D models piled up along ridge-axis with their own M . (IMPORTANT: this suggests the importance and urgence for making clear conclusion and results description for previous pseudo-2D models results. However, one difficulty here is that the characteristic fault offset ΔX_c is different

between 2D and 3D models.)

4.1 Discussion on Reference models

4.1.1 Location of termination (M28LinT1)

The location of the termination of the detachment fault where footwall begins to be exhumed to the surface varies along the ridge-axis (i.e. Z-axis). As shown in Figure 24, the highest strain rate regions (red) can be interpreted as detachment fault interfaces. When $M \leq 0.5$, although the rate of fault slip should be higher for lower M, the rate of bending or decreasing in dip angle of the fault has a maximum value corresponds to the far field extension rate. Because for $M < 0.5$, the detachments root at the same place (center dike at a depth five to six elements beneath the surface)(Figure 24.Z=0, 5, 10) along the ridge-axis, the amount of bending in the footwall of the detachment is determined by the amount of the displacement of the breakaway. In other words, because in order to spend least frictional energy during faulting, fault interface between the two ends (breakaway and root) tends to be a straight line. Thus, the dip angle of the fault is inverse proportional to the distance between the breakaway and the root of the normal fault when $M < 0.5$. So the further between the breakaway and the root of the fault, the lower its dip angle. Since the breakaways at the region with $M < 0.5$ is pulled with the same velocity V_x , the distances between the breakaways and the roots of the faults are the same. Thus the dip angles of the faults at the same time along the ridge-axis are the same. However, when $M > 0.5$, the amount of fault slip decreases as M increase and the crust at the footwall experiences less bending and the detachment remains in high angle with closer to ridge-axis termination (Figure 24.Z=15, 20). This is due to the root of the fault is being slowly pushed away from ridge-axis while the breakaway of the fault is closer to ridge center since the fault initiates later than that at the low M side. In addition, the crust thickness that the fault cuts through is slowly increasing as the fault being pushed away from ridge center due to excessive diking. These three factors together contribute to a higher dip angle. In a unit time, the volume of the

exhumation is also smaller for the higher M side. One thing needs to be noted that the lowest topography points at high M side correspond to the terminations but detached from the terminations at the low M side ($M < 0.5$) as shown in Figure 24.

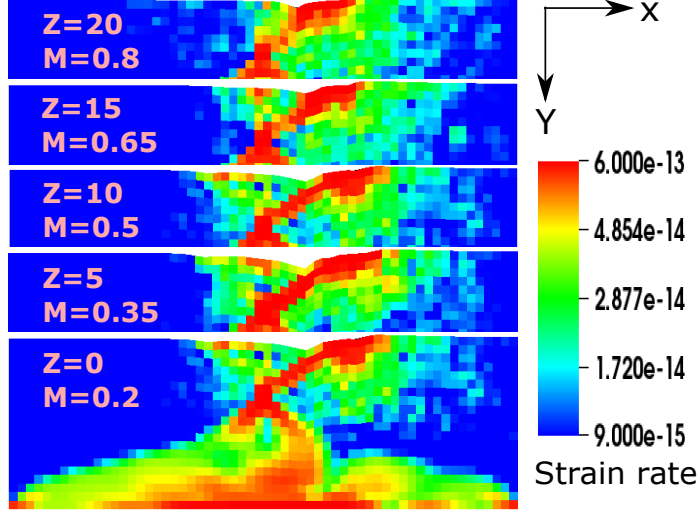


Figure 24: M28LinT1 (Table 2). Strain rate at 107.5kyr with five slices along ridge axis(Z axis).

4.1.2 Shear low (M28LinT1)

The lowest topography points inside the median valley evolves from a straight line parallel to the ridge-axis (Figure 25.a) to a line oblique to the ridge-axis (Figure 25.b,c,d). Initially, the lowest topography points are at the terminations of the detachment fault. Due to the coupling along the ridge-axis, fault propagates from front to back in a straight line parallel to the ridge-axis. However, as the dip angle of the detachment at the low M side begin to decrease due to bending of the crust at the footwall, along with excessive tensional stress results from low magma supply, the lowest topography point at the lower M side is pulled to the conjugate plate. While the lowest topography points at the high M side ($M > 0.5$) are pushed away from the dike. Note that the oblique lowest topography points form not a straight line, but a curve that the lowest point remains near the ridge-axis at the high M side. This is due to the bending rate of the detachment at high M side is very low and thus the termination can remains near the ridge-axis. *^{XT}:One question needs to be answered: at*

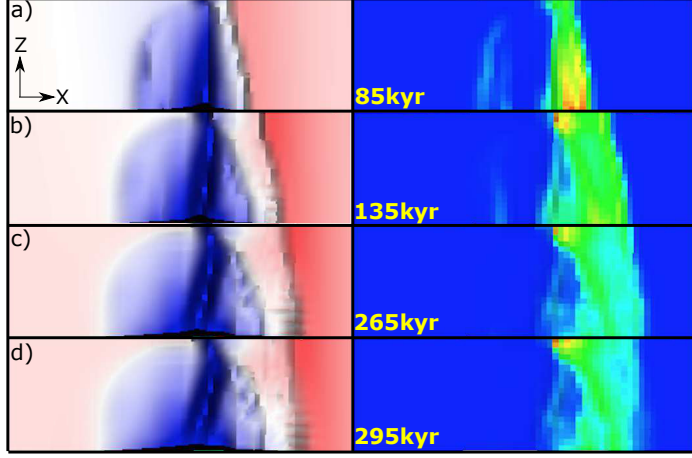


Figure 25: M28LinT1 (Table 2). Breakaway evolution through time. Viewing from top. Left column is topography at different time; Right column is plastic strain. They both share same color scales in the figure 8. The offset between breakways along the ridge-axis in X-axis direction remains three elements until time 295kyr. It also shows that the lowest topography points along the ridge-axis start as a straight line parallel with ridge-axis in a) and then gradually become oblique to the ridge-axis. Please see text for detail description.

410 timesteps (205kyr), the breakaway at the front already extends 15km. If assuming a constant extending rate, it means a velocity of around 75km/Myr, much faster than half spreading rate 25km/Myr. If it is true, I need to change previous discussion on how fast breakaway being pulled away from ridge-axis.

4.2 Cut Back

The cut back happens mostly in the square root model. Since the linear model and the square root model have more obvious difference in terms of the cut back behavior, here, we only compare linear and square root. There are several factors contribute to the cut back behavior. First, at the higher M side, the amount of diking for the square root model is ubiquitously larger than that of the linear one (Figure 10). This leads to a slower bending detachment at the high M side for the square root model. Second, the total length of the ridge segment with $M > 0.5$ for the square root model is also longer than that of the linear one (Figure 10). This results in that at the low M side, σ_{xz} is focused at low Z adjacent to the ridge-axis (Figure 12.e), however for linear is spread out to Z higher than 10. Third,

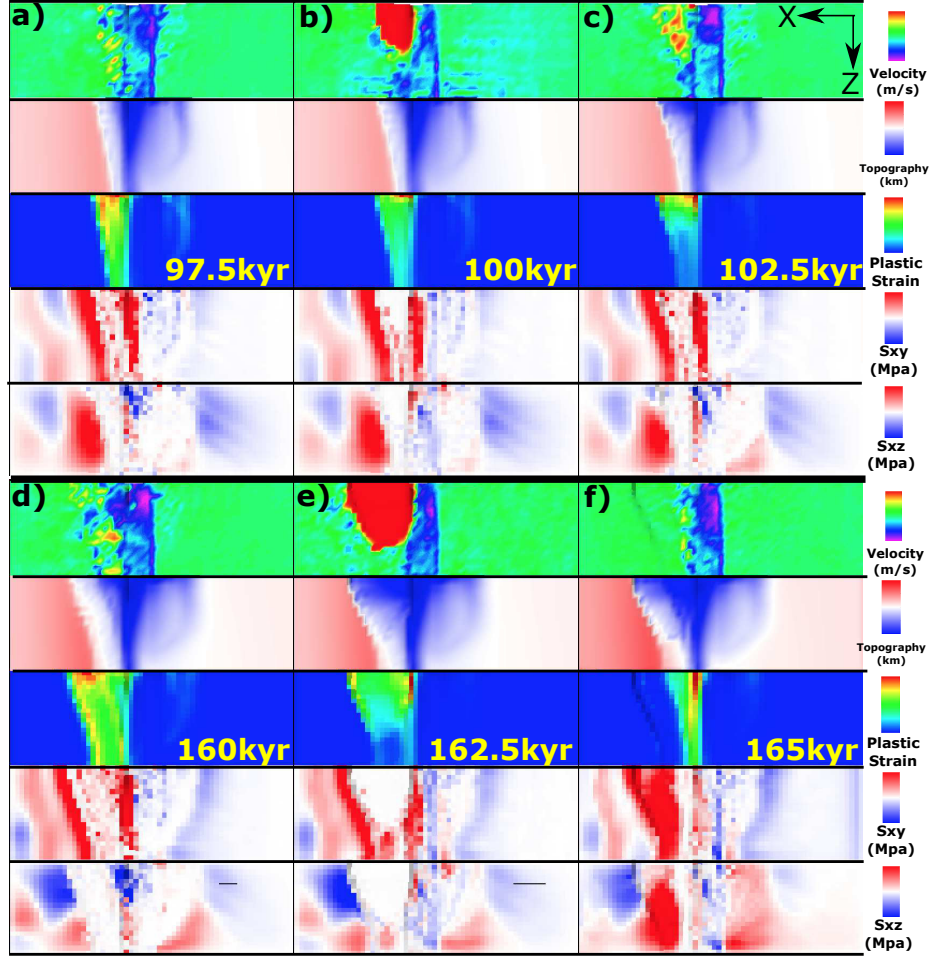


Figure 26: M28SqrtT1 (Table 2). Cut back behaviors in square root functional form model with different time.

due to higher value of $\frac{dM}{dZ}$ for square root when $Z < 5$, the along ridge-axis shear σ_{xz} for square root will be accumulating faster, which produces larger strike-slip force to cut the hanging wall at the low M side. Fourth, as observed in the model (Figure 12.c), the parallel to spreading direction offset between breakaways along the ridge-axis is 4km for the square root model compared to 3km for the linear model. This causes the square root model to experience bigger shear stress σ_{xy} both immediately beneath and above the fault interface at the low M side (Figure 12.d). Fifth, as shown in Figure 28, due to bending of the crust at the footwall side, below the blue neutral plane, $\sigma_{xx} > 0$, meaning tensional stress being accumulated as fault develops. The resulting force tends to unbend the bent crust and drag down the connecting surface (the future decoupled hanging wall). All five

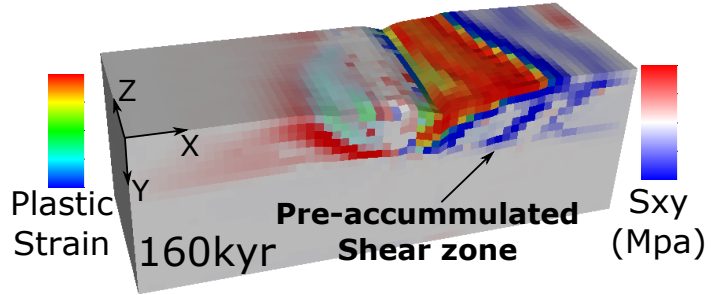


Figure 27: M28SqrtT1 (Table 2). Square root functional form model at 160kyr. Pre-accumulated shear zone increase the shear force and cut the weak detachment front tip

factors together assist in the decouple of the hanging wall at the low M side as described in detail in the next paragraph.

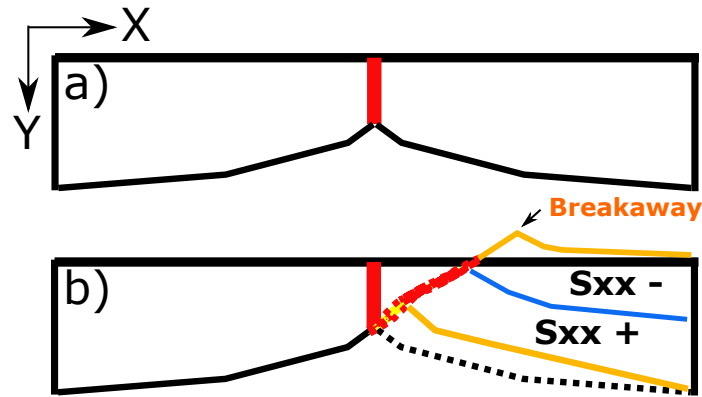


Figure 28: Bending stress illustration. The blue line is the neutral plane where $\sigma_{xx} = 0$. Above the neutral plane is compression and beneath it is tension. Due to sea water pressure and lithostatic pressure, compression is generally one degree magnitude larger than tension.

In the Figure 26, the hanging wall rebounds backwards to the dike in a high velocity (Figure 26.b,e (velocity)) accompanied with a sudden topography drop (Figure 26.b) compared to c); d) compared to e) (in the second row)). This behavior is triggered when the front tip of the weak detachment extends further away from the ridge-axis and reaches a pre-accumulated shear zone (Figure 27). The pre-accumulated shear zone adds extra shear force to the weak (Figure 26.d(third row: plastic strain)) as well as shear stresses accumulated (Figure 26.d(fourth and fifth row: σ_{xy} and σ_{xz})) fault interface and together with the five factors mentioned in the previous paragraph result in the cut back behavior. The cut back produces a continuous high angle fault scarp with a relief of $\sim 1\text{ km}$ aligns

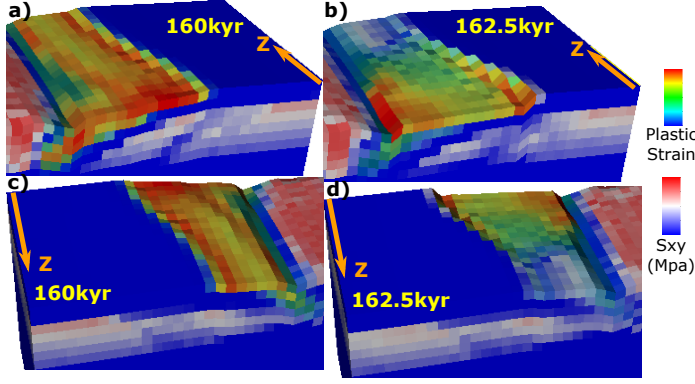


Figure 29: M28SqrtT1 (Table 2). Bending stress drop in the crust close to dike due to cut back behavior.

to the initial breakaway and extends for about 20 kilometer in length (Figure 26.e (second row: topography)). Its distance to the ridge-axis varies along the Z-axis and this result can be used to indicate the magma supply variation in the nature. ^{XT:}To be discussed in observation comparison section. as a reminder

During the cut back process, the tensional bending stress are released at the low M side ($0 < Z < 7$) in the left tip of the bended crust (Figure 29.a compared to b), however, in the higher M side, the tensional bending stress keeps accummulating due to the far field extension (Figure 29.c compared to d). This behavior assists in the decouple between low M and high M side hanging walls.

Once the cut back happens at 162.5kyr, the σ_{xy} , σ_{xz} and σ_{xx} are released (Figure 26.e (fourth and fifth row: σ_{xy} and σ_{xz})). The plastic strain near the ridge-axis at low M side reaches a maximum of ~ 0.9 (Figure 26.e (third row: plastic strain)) compared to ~ 0.3 before and after. This is due to the sudden backward motion squeezes the end element of the hanging wall near the ridge-axis and later be released by the continuous extension.

After the cut back, the termination of the detachment recedes backwards for about 7 kilometer towards the ridge-axis (Figure 26.f (third row: plastic strain)) (termination fronts are always consistent with tension stresses in σ_{xx} and σ_{zz} as well as with plastic strain front(due to healing, high plastic strain region corresponds only to region with continuously deformation) (Figure 12 and Figure 13)). This behavior helps maintain a high angle normal

fault. Different from the linear and sinusoidal models that the detachments at the low M side will rotate to a very low angle, square root model doesn't. In addition, σ_{xy} and σ_{xz} soon fill in the area between cut back created fault scarp and the new termination (Figure 26.f (fourth and fifth row: σ_{xy} and σ_{xz}) because σ_{xy} always accumulates immediately beneath the normal fault interface and the red σ_{xz} left to the new termination is due to the along ridge-axis variation in the rate of fault slip (low M side larger).

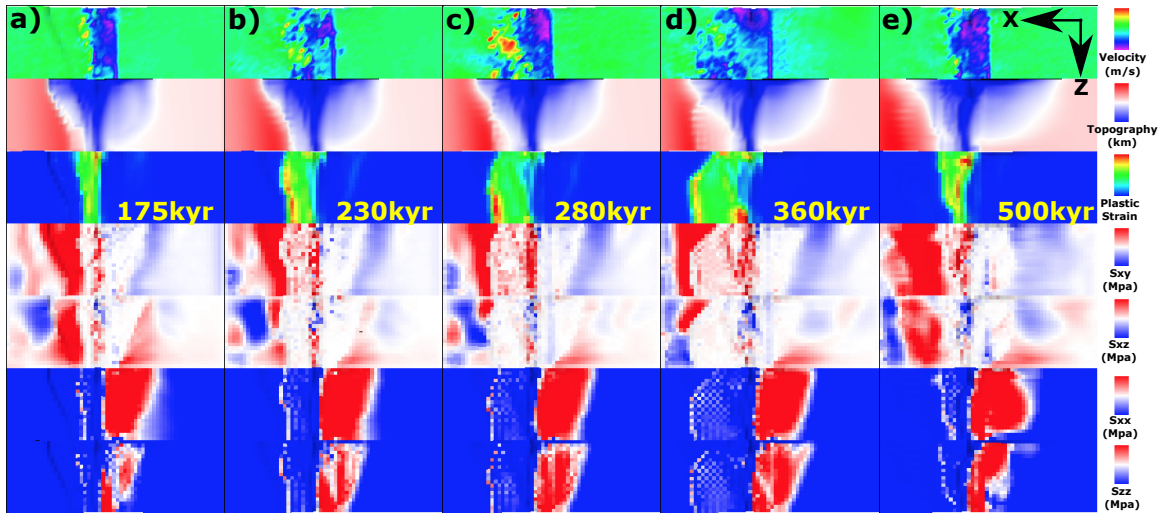


Figure 30: M28SqrtT1 (Table 2). New fault front chase after initial abandoned breakaway.

There is one phenomenon very interesting and counter-intuitive that worth describing here. After the cut back, and termination retreat, the evolution of the detachment fronts is opposite to initial or to the general behavior in the linear and sinusoidal models. The termination front at the high M side extends faster and further after the cut back (Figure 30). This is partly related to the unbending decouple phenomenon we described earlier that the tensional stress are released at the low M side but continues to accumulate in the high M side during the cut back unbending in the low M side. Since the tensional stress is released in the low M side, it needs time to accumulate to where it was and then start from there to drag the new near ridge-axis fault away from the ridge-axis while at the high M side the increasing tensional stress will directly lead to a fast extending fault front. Thus create the behavior. *XT: One question is, how to explain that the fault front is moving much*

faster than the initial abandoned breakaway? New fault front soon reach the old breakaway.

This phenomenon is largely responsible for the corrugations observed. It creates a “X” shape “scan” that first “scan” the topography with faster low M side (Figure 26.d and e) and then with faster high M side (Figure 30.c and d). This results in curved terminations with hundreds to several kilometers wavelengths that directly create parallel to spreading direction corrugations.

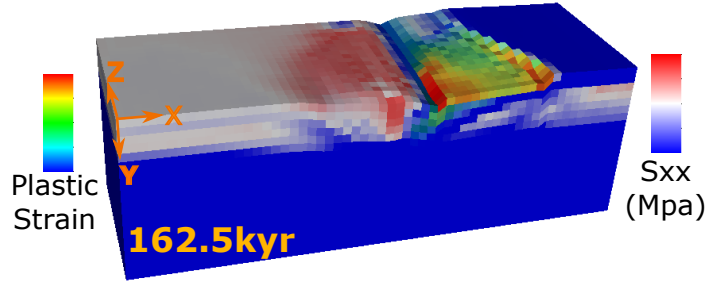


Figure 31: M28SqrtT1 (Table 2). Higher σ_{xx} in the median valley of conjugate plate at low M side.

In addition, the higher σ_{xx} in the median valley of conjugate plate at low M side (Figure 31) is due to the brittle crust is thinnest at the median valley, thus when same amount of force propagates from far field extension to the center median valley, the stress will increases.

4.3 Faulting Patterns Evolution

4.3.1 Trade-off between bending and weakening

Before we move on to each of the pairs, the framework studied by [Lavier et al., 2000] needs to be mentioned here for better understanding the model behaviors observed in our model results. There is a trade-off between change in bending force ΔF_b as a function of fault offset ΔX and force change ΔF_w as a function of ΔX due to strain weakening. As described in [Lavier et al., 2000], higher characteristic fault offset (ΔX_c) or slower strain weakening results in multiple faults rather than only one fault lasting. Whether conjugate fault and even multiple faults can be produced depends on the local stress condition. The

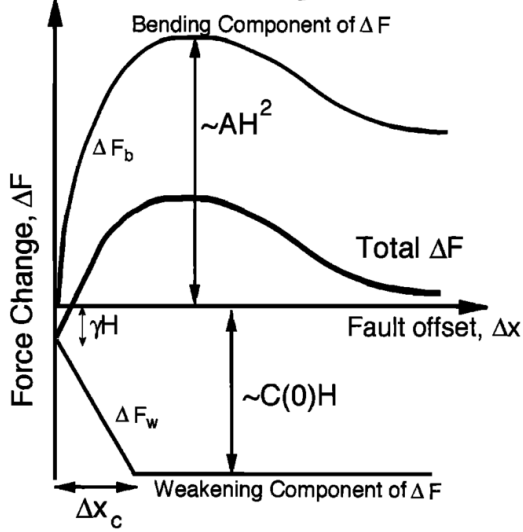


Figure 32: Trade-off between change in bending force ΔF_b and weakening in the fault interface ΔF_w . H is the thickness of the brittle crust and γ is the size of initial weak perturbation and A defines the maximum bending force change. (For more details, please refer to [Lavier et al., 2000])

strength weakening of the existed fault combines with how much bending force resists the fault to keep offsetting play a major role in determining the stress state at the other areas. As the sea-floor keeps spreading and ΔX increasing, the change in bending force ΔF_b increases and the strength at the fault interface decreases due to weakening ΔF_w (Figure 32). If the net force change $\Delta F = \Delta F_b + \Delta F_w$ is positive, it means that it is getting harder and harder to maintain the existing fault and stress will begin to accumulate at the other areas which eventually break another fault. ΔF_b initially increases fast with respect to ΔX and then when the breakaway bends over, it reaches its peak value and begin to decreases a little and maintains at a constant value. If the strain weakening is fast enough that the net effect force ΔF is always negative, then most of the stress will be released by the existing fault and thus no conjugate or multiple faults will be created.

Our model results verify this analysis that only Type two weakening (slower weakening with higher ΔX_c) can produce an alternating normal fault on the conjugate plate.

4.3.2 Alternating on conjugate plate

The fault alternation behavior observed in pseudo-2D models in cases $M > 0.5$ is much more complicated in 3D models. The results shows that only Type two weakening with M58 will result in a alternating faulting pattern. ^{XT:}integrate the area of $M > 0.5$ with respect to Z to see if there is any quantatative analysis available.

4.3.3 Secondary near-axis normal fault

The secondary near axis high angle normal fault is another common observation of the models. As shown in Figure 8, at the ridge axis with $M > 0.5$ (i.e. $Z > 10$), the existing normal fault will be pushed away from the ridge-axis due to excessive diking, as its mechanism has been mentioned in the introduction chapter, another new near axis normal fault is created at around 650kyr. As it evolve, the initial detachment fault become inactive (the transparent view of plastic strain shown in the rigth corner inset of time 880kyr). This secondary fault creates another dome and its composition is more likely to be volcanic rather than ultramafic, however, as is evolve, if it can last long, lower crust and upper mantle material can be exhumed to the surface. The composition of the domes observed at Kane magamullions is similar to this mechanism that ultramafic Babel dome is on the West and crustal inside-corner high on the East.

4.4 Corrugations

There are two contributing factors, for one, trans-extenstional stresses are created due to offset of the breakaway as well as the variation in fault displacements along the ridge axis; for the other, the variation of the positions of the terminations of the detachment faults along the ridge-axis creates anastomosing faults that is mentioned in [Smith et al., 2014]. This anastomosing faulting behavior is largely responsible for corrugations in our models.

The stress at the tips of the breakaways is generally tensional in both parallel and or-

thogonal directions to the ridge-axis. (Figure 12.f,g)

4.4.1 Wavelength of corrugations

4.5 Influence of healing

4.6 Comparing model results with nature observation

4.7 Parallel computing efficiency

4.8 Model Limitation

4.8.1 Fixed thermal structure effects and justification

Thermal conduction rate for $\kappa = 6\text{mm}^2/\text{s}$ material is $1.8\text{e}5 \text{ km/Myr}$, four magnitude faster compared to spreading rate of 2.5km/Myr .

4.9 Reccommendation for Future Research

5 Conclusions

References

- G. Baines, M. J. Cheadle, B. E. John, and J. J. Schwartz. The rate of oceanic detachment faulting at atlantis bank, sw indian ridge. *Earth and Planetary Science Letters*, 273(1-2):105–114, Aug. 2008. ISSN 0012821X. doi: 10.1016/j.epsl.2008.06.013.
- R. Buck, L. Lavier, and A. Poliakov. Modes of faulting at mid-ocean ridges. *Nature*, 434(7034):719–23, 2005. ISSN 1476-4687. doi: 10.1038/nature03358.
- S. M. Carbotte, D. K. Smith, M. Cannat, and E. M. Klein. Tectonic and magmatic segmentation of the global ocean ridge system : a synthesis of observations. *Geological Society of London*, 2015.
- Y. J. Chen and J. Lin. Mechanisms for the formation of ridge-axis topography at slow-spreading ridges: A lithospheric-plate flexural model. *Geophysical Journal International*, 136:8–18, 1999. ISSN 0956540X. doi: 10.1046/j.1365-246X.1999.00716.x.
- E. Choi, L. Lavier, and M. Gurnis. Thermomechanics of mid-ocean ridge segmentation. *Physics of the Earth and Planetary Interiors*, 171(1-4):374–386, Dec. 2008. ISSN 00319201. doi: 10.1016/j.pepi.2008.08.010.
- C. M. R. Fowler. *The solid earth: an introduction to global geophysics*. Cambridge University Press, 2004.
- S. Kirby and A. K. Kronenberg. Rheology of the lithosphere: Selected topics. *Reviews of Geophysics*, 25(6):1219–1244, 1987.
- L. L. Lavier, W. R. Buck, and A. N. B. Poliakov. Factors controlling normal fault offset in an ideal brittle layer. *Journal of Geophysical Research*, 105(B10):23431, 2000. doi: 10.1029/2000JB900108.
- J. Lin, G. M. Purdy, H. Schouten, J.-C. Sempere, and C. Zervas. Evidence from gravity

data for focused magmatic accretion along the Mid-Atlantic Ridge. *Nature*, 344:627–632, 1990. ISSN 0028-0836. doi: 10.1038/344627a0.

W. B. F. Ryan, S. M. Carbotte, J. O. Coplan, S. O’Hara, A. Melkonian, R. Arko, R. A. Weissel, V. Ferrini, A. Goodwillie, F. Nitsche, J. Bonczkowski, and R. Zemsky. Global multi-resolution topography synthesis. *Geochemistry, Geophysics, Geosystems*, 10, 2009. ISSN 15252027. doi: 10.1029/2008GC002332.

D. K. Smith, H. Schouten, H. J. B. Dick, J. R. Cann, V. Salters, H. R. Marschall, F. Ji, D. Yoerger, A. Sanfilippo, R. Parnell-turner, C. Palmiotto, A. Zhelezov, H. Bai, W. Junkin, B. Urann, S. Dick, M. Sulanowska, P. Lemmond, and S. Curry. Development and evolution of detachment faulting along 50 km of the mid-atlantic ridge near 16.5°n. *Geochemistry Geophysics Geosystems*, pages 4692–4711, 2014. doi: 10.1002/2014GC005563. Received.

M. Tolstoy, A. J. Harding, and J. A. Orcutt. Crustal Thickness on the Mid-Atlantic Ridge: Bull’s-Eye Gravity Anomalies and Focused Accretion. *Science*, 262(October):726–729, 1993. ISSN 0036-8075. doi: 10.1126/science.262.5134.726.

B. E. Tucholke, M. D. Behn, W. R. Buck, and J. Lin. Role of melt supply in oceanic detachment faulting and formation of megamullions. *Geology*, 36(6):455, 2008. ISSN 0091-7613. doi: 10.1130/G24639A.1.

D. L. Turcotte and G. Schubert. *Geodynamics*. Cambridge, 2002.